https://doi.org/10.5194/egusphere-2026-921
Preprint. Discussion started: 18 May 2026

Mineralogical composition of transported desert dust over Cabo Verde and comparison with model predictions

Maria Tsichla[1,2], Konrad Kandler[3], Sudharaj Aryasree[3], Stavros Solomos[4], Christos Spyrou[4], Alexandra Tsekeri[1], Anna Kampouri[1], Anna Gialitaki[1], Eleni Drakaki[1,5], Thanasis Natsis[1], Maria Kezoudi[6], Alkistis Papetta[6], Franco Marenco[6], Jean Sciare[6], Eleni Marinou[1], Kalliopi-Artemis Voudouri[1,7], Nikos Mihalopoulos[1,2], and Vassilis Amiridis[1]

[1]National Observatory of Athens, IAASARS, Greece
[2]Environmental Chemical Processes Laboratory, Department of Chemistry, University of Crete, Greece
[3]Institute of Applied Geosciences, Technical University of Darmstadt, Darmstadt, Germany
[4]Research Centre for Atmospheric Physics and Climatology, Academy of Athens, Greece
[5]Department of Geography, Harokopio University of Athens, Greece
[6]Climate and Atmosphere Research Centre, The Cyprus Institute, Nicosia, Cyprus
[7] Laboratory of Atmospheric Physics, Physics Department, Aristotle University of Thessaloniki, Greece

Correspondence to: Maria Tsichla (mtsichla@noa.gr)

Abstract. The mineralogical and chemical composition of desert dust particles strongly influences their cloud-forming ability and radiative effects. This study provides quantitative estimates of the main mineralogical and elemental components of desert dust during atmospheric transport above Cabo Verde based on in-situ measurements from the ASKOS campaign in summer 2022, obtained using impactors mounted on unmanned aerial vehicles. Simulations from the METAL-WRF model were used for comparison with sun-photometer observations of total dust load and with in-situ measurements of relative elemental mass fractions of key elements. Across all cases, particle chemical signatures were dominated by illite/muscovite (62%), followed by smectite (9%), kaolinite (9%), quartz (7%), feldspar (5%), calcite (4%), gypsum (3%), and Fe-oxide/Fe-hydroxide (1%). Trajectory and source–receptor analyses combined with satellite observations revealed enhanced calcite fractions for air-masses originating from northern Mali, whereas air masses from southern Mali exhibited increased proportions of Fe-oxide/hydroxide. Good agreement was found between METAL-WRF-derived total dust mass concentrations and independent AERONET observations (slope = 0.62, r = 0.87). Based on in-situ measurements, Si was the dominant elemental component (~25%), followed by Al (~12%), Fe (~6%), Ca (~2.7%), and S (~0.4%). While METAL-WRF reproduced the mean relative abundances of Fe and Ca over the 20-day period, it did not capture the case-to-case variability. Nevertheless, Fe exhibited good agreement, within overlapping uncertainty, between modelled and measured values for most cases, which is particularly relevant for studies of ocean biogeochemistry and dust-related radiative processes.

https://doi.org/10.5194/egusphere-2026-921
Preprint. Discussion started: 18 May 2026

1 Introduction

The mineralogical and chemical composition of desert dust particles plays a key role in the Earth's system. Desert dust minerals demonstrate distinct functions regarding their ability to form cloud droplets and ice crystals (DeMott et al., 2003; Weger et al., 2018; Zimmermann et al., 2008), interact with soluble gases (Chen et al., 2020; Hanke et al., 2003; Matsuki et al., 2005), and promote heterogeneous reactions with reactive gases (Bauer et al., 2004; Hanisch & Crowley, 2003). The differences are mostly driven by their surface properties, which are defined from their chemical composition, their production processes—milling, and their ability to uptake water (Gustafsson et al., 2005).

For example, silicates, and in particular quartz, tend to be less effective cloud condensation nuclei (CCN) than clay minerals, such as montmorillonite and illite (Hatch et al., 2014; Kumar et al., 2011). This is due to the fact that clay minerals have a porous structure and rough surfaces, which provide more sites for gas adsorption compared to the relatively smoother surfaces of larger silicate particles. Also, feldspars, and especially potassium-rich feldspars (K-feldspars), have been identified as key species controlling the ice-nucleating (IN) activity of airborne desert dust (Atkinson et al., 2013; Yakobi-Hancock et al., 2013), most likely being more reactive with water (Fenter et al., 2000). In addition to surface morphology, the elemental composition also plays a role, as higher Na/Si and Ca/Si ratios increase the relative humidity threshold required for water-monolayer formation. Based on these properties, African desert dust is generally more hydrophilic than Asian desert dust (Joshi et al., 2017). The studies assessing these parameters rely on different methods and assumptions so the results may vary across the literature. A comprehensive review of these findings is provided by Tang et al. (2016).

In addition, dust particles interact with radiation either directly, by scattering and absorbing light, or indirectly, through their effect on clouds. Observations suggest that models tend to underestimate the absorption of solar radiation by mineral dust (Adebiyi et al., 2023; Fountoulakis et al., 2024). The dust's content of iron oxides—primarily—and subsequently of hematite, Fe, and goethite, plays a key role in determining the particle's refractive index and single scattering albedo (Di Biagio et al., 2019), and thereby its direct radiative effect (Li et al., 2021). Laboratory and field studies have reported the optical properties of individual minerals such as quartz, feldspar, silicates, and phyllosilicates across the ultraviolet to thermal infrared range (Glotch et al., 2007; Herbin et al., 2023; Hubert et al., 2017; Laskina et al., 2012). Incorporating these mineral-specific optical properties into models can significantly improve predictions of scattering, transmission, and absorption processes in the atmosphere, and decrease the uncertainty in quantifying the radiative effect of desert dust (Fountoulakis et al., 2024).

Finally, the deposition of key elements on forests and oceans changes the nutrient balance and biogeochemical cycles of the ecosystems. Particularly iron, acts as a limiting micronutrient for phytoplankton growth, thereby impacting the global carbon cycle (Drenkard et al., 2023; Jickells et al., 2005; Mahowald et al., 2005).

Due to the different properties and functions of the desert dust minerals, it is important to account for their presence and abundance. Over the past decades, numerous field campaigns and long-term ground-based observations have been conducted across West Africa to investigate the mineral and chemical composition of desert dust from Sahara (Formenti et al., 2014; Kandler et al., 2007; Lieke et al., 2011), the biggest dust source of the world (Prospero et al., 2002). Among the most recent

https://doi.org/10.5194/egusphere-2026-921
Preprint. Discussion started: 18 May 2026

efforts is the ASKOS ESA campaign in Cabo Verde (Marinou et al., 2023), conducted during the summers of 2021 and 2022, providing measurements on elevated Saharan dust layers using ground-based and satellite remote sensing, as well as in-situ observations with Unmanned Aerial Vehicles (UAVs). This approach enabled a detailed characterization of the physical and chemical properties of transported desert dust.

Such observations are critical for evaluating and constraining dust models, which can be used to investigate key atmospheric processes, by complementing the gaps of the limited spatial and temporal coverage of measurements. Models that explicitly provide the desert dust mineralogical composition are typically based on the framework of Claquin et al. (1999), which classifies desert dust into mineral groups such as illite, kaolinite, smectite, hematite, calcite, feldspar, quartz, and gypsum. Their validation has been primarily done using ground-level in-situ measurements of mineralogical composition (Pérez García-Pando et al., 2016; Perlwitz et al., 2015; Solomos et al., 2023; Song et al., 2024). This study presents a first attempt to validate the derived elemental composition of desert dust during atmospheric transport at various altitudes above Cabo Verde from the METAL-WRF model (Solomos et al., 2023), using in-situ measurements from free-stream impactors mounted on UAVs. Model outputs were also compared with AERONET sun-photometer retrievals. To our knowledge this is the first time that such combination between measurements using UAVs and models is performed worldwide.

The structure of the paper is outlined below. Section 2 presents an overview of the campaign, the experimental techniques employed, and the methodologies applied both for the measurements and model. Section 3 presents the results, starting with the atmospheric conditions during the campaign and the analyzed cases, followed by the mineralogical composition of the desert dust particles, and the comparison of AERONET and in-situ observations with METAL-WRF outputs in terms of total columnar mass and elemental mass percentages. Finally, Sect. 4 summarizes the main findings of the study.

2 Campaign description and experimental methods

2.1 Overview of the ASKOS campaign

The ASKOS ESA campaign was carried out on São Vicente Island, Cabo Verde, during the summers of 2021 and 2022. It served as the ground-based component of the Joint Aeolus Tropical Atlantic Campaign (JATAC), organized by ESA and NASA (Fehr et al., 2023), with the main objective of the calibration and validation of the Aeolus satellite mission, with a particular emphasis on aerosol-related products.

The campaign employed multi-platform observations, including ground-based, airborne, and in-situ measurements. Various instruments were used across the São Vicente Island, with most of them deployed at the Ocean Science Centre Mindelo (OSCM) and its surrounding area. These included lidars, cloud radars, sun photometers, a microwave radiometer, electric field sensors, and in-situ instruments onboard UAVs. ASKOS observations provided a wealth of information regarding microphysical aerosol properties (e.g., size distribution, shape, composition), vertically-resolved and columnar aerosol optical properties, reflectivity and doppler velocity of targets in the line of sight of the radar, wind velocity, solar and infrared

https://doi.org/10.5194/egusphere-2026-921
Preprint. Discussion started: 18 May 2026

irradiance, and atmospheric electric fields to support the validation of satellite retrievals and facilitate detailed investigations of aerosol–cloud–radiation interactions, focusing on desert dust. More details can be found in Marinou et al. (2023).

2.2 Experimental techniques

2.2.1 In-situ measurements

The in-situ measurements were acquired with unmanned aerial vehicles (UAVs; Fig. 1a,b) operated by the Cyprus Institute at the Cesária Évora International Airport (Kezoudi et al., 2021), and remotely piloted from a ground control station. This flight setup enabled direct sampling of atmospheric aerosols while minimizing disturbance to ambient atmospheric conditions (Bieber et al., 2020; Burgués & Marco, 2020; Cheng et al., 2023; Crazzolara et al., 2019). The UAVs were equipped with free-stream impactors mounted on an adjustable arm and insulation casing, enabling aerosol collection at selected altitudes and specified sampling durations for offline analysis (Fig. 1c). In total, 25 flights were conducted, 12 during the day and 13 at night, having impactors on-board, sampling both within and below the dust layers to provide vertical profiles of aerosol properties.

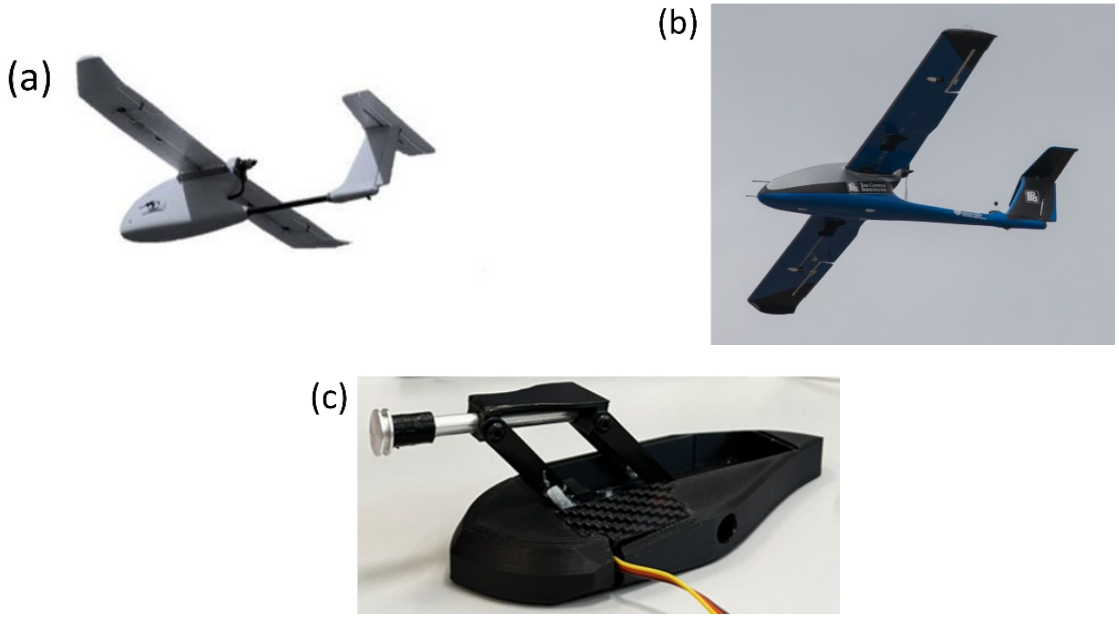

Figure 1. (a) "Skywalker 2015" and (b) "CoBi" Unmanned Aerial Vehicles, designed for carrying cameras, sensors and equipment. (c) Free-stream impactor for particle sampling.

The free-stream impactor is based on a design developed for a fast-flying research aircraft (Lieke et al., 2011) and has been adapted to the drone operation (Kezoudi et al., 2021). Particles are directly collected due to their inertia on a pure-carbon adhesive (Plano SpectroTabs, Plane GmbH, Wetzlar, Germany). The collection efficiency of the impactor relative to the Universal Cloud and Aerosol Sounding System (UCASS; Smith et al. (2019)) varies with particle diameter, increasing from approximately 0.1 at ~1 μm to unity between 4 and 14 μm, and subsequently decreasing to about 0.4 for particles larger than

https://doi.org/10.5194/egusphere-2026-921
Preprint. Discussion started: 18 May 2026

15 µm (Kezoudi et al., 2025). Since the campaign had a special focus on desert dust the UAV flights were scheduled during dust events according to dust forecasts, and the impactors collected samples mainly within the Saharan Air Layer (SAL; at 1.5-5 km) (Ryder et al., 2013). The sampling times were adjusted, based on the estimated aerosol concentration, and ranged between 4 and 6 min.

2.2.2 Free-stream impactor analysis

Without any further treatment, particles were analyzed by scanning electron microscopy (SEM; 400 FEG, FEI, Eindhoven, The Netherlands) with Energy-dispersive X-ray spectroscopy (EDX; Oxford X-Max 120, Oxford Instruments, Abingdon, United Kingdom) to determine particle morphology and composition. Sample analysis was performed semi-automatically. Particle areas were segmented from the substrate background by a brightness threshold in the instrument-specific image analysis system (Oxford Aztec 6.2) based on the backscatter electron image. Afterwards, the identified particles were scanned by the electron beam, and the emitted X-ray radiation was collected for around 5 seconds, yielding 150,000 X-ray counts. From the characteristic peaks, using the instrument software-inherent quantification scheme, the composition of the particles was determined. Elements with lower Z than oxygen were excluded from the analysis, as they are present in the substrate and their quantification is extremely uncertain. For more details refer to Kandler et al. (2018). Approximately 26,000 individual particles were analyzed.

Chemical elements present in atmospheric dust particles typically occur in the form of oxides. For example, in case of iron we assume the more common form Fe^{3+}. To estimate the mass fraction of each element in the sample, the oxide weight is calculated by stochiometric masses and, subsequently, the mass of an element in each particle. The total particle mass is estimated from its cross section visible in the microscope (Kandler et al., 2018), yielding a volume and an average density for the different mineral groups of 2.65 g cm^{-3} (Kandler et al., 2007), consistent with the value reported for dust by Hess et al., 1998.

Uncertainties were estimated using the bootstrap resampling method, providing the central 95% confidence interval bounds (lower and upper) for each value (Efron, 2003; Kandler et al., 2018).

Particles were further classified into mineral groups corresponding to the minerals represented in the model using a conversion table that relates the relative abundances of major desert dust elements to specific mineral phases (Table 1). This table reports normalized elemental mass fractions of the corresponding minerals after excluding oxygen, following the approach of Kandler et al., 2007. Assignment was performed by calculating the Euclidean distance between each particle's elemental composition and the characteristic elemental compositions of the considered mineral groups. Each particle was assigned to the closest group.

Table 1. Conversion table linking key minerals to the average relative composition of major desert dust elements (excluding oxygen).

Mineral/Chemical elements	Na	Mg	Al	Si	S	K	Ca	Ti	Fe

https://doi.org/10.5194/egusphere-2026-921
Preprint. Discussion started: 18 May 2026

Quartz-like				1					
Kaolinite-like			0.487	0.49				0.023	
Illite/ Muscovite-like		0.027	0.219	0.539		0.091	0.031	0.008	0.086
Smectite-like		0.03	0.211	0.673			0.023		0.063
Feldspar-like	0.021		0.24	0.543		0.11	0.085		
Calcite-like							1		
Gypsum-like					0.445		0.555		
Fe-oxide/ Fe-hydroxide-like			0.055	0.036					0.909

145

2.3 Model description

Simulations using the METAL-WRF model (Solomos et al., 2023; Spyrou et al., 2025) were performed, providing estimates of the total desert dust load and the mass concentration of key chemical elements (Si, Fe, Ca, Al, and S), over Cabo Verde during the campaign period. The METAL-WRF model is based on the Weather Research and Forecasting (WRF) model
150 (Skamarock et al., 2021) coupled with the Chemistry (Chem) module (Grell et al., 2005). This configuration enables the representation of various atmospheric chemical species and aerosols, including desert dust. The parameterization of dust emission, transport and deposition schemes followed (LeGrand et al., 2019) and (Seinfeld & Pandis, 1998), and more recent modeling developments by (Solomos et al., 2011, 2023; Spyrou et al., 2010, 2025; Tsarpalis et al., 2018).

The mineralogy module is based on the classification of aerosol emission regions as "dust-productive soils" (Engelstaedter &
155 Washington, 2007; Nickovic et al., 2012), along with the estimation of their mineral content. The selection of key minerals and chemical elements used to represent these soils (i.e., quartz, feldspar, gypsum, illite, kaolinite, smectite, hematite, calcite, and iron) is based on their abundance, optical characteristics, and chemical properties (Claquin et al., 1999; Nickovic et al., 2013). Finally, minerals are converted to their corresponding chemical elements according to Table A1 of the Appendix.

The model domain is shown in Fig. A1 covering tropical to mid-latitude regions to encompass a wider range of atmospheric
160 transport pathways. The model is set up with a resolution of 22.5 Km × 22.5 Km and 32 vertical hybrid-sigma levels stretching from the surface to the top of the atmosphere. Initial and boundary conditions are from the ERA5 dataset (Hersbach et al., 2020), and the physical parameterizations used in these simulations are shown in Table A2.

2.4 Backward transport analysis supported by satellite observations

The HYbrid Single-Particle Lagrangian Integrated Trajectory (HYSPLIT) model (Stein et al., 2015) was used to calculate
165 backward air-mass trajectories for each case. An 8-day integration period was selected, consistent with the typical 7–10 day atmospheric residence time of tropospheric mineral dust (Knippertz & Stuut, 2014). This duration is sufficient to identify

https://doi.org/10.5194/egusphere-2026-921
Preprint. Discussion started: 18 May 2026

dominant source regions and characterize large-scale transport pathways, while limiting the influence of short-lived, transient meteorological features. For each case, trajectories were initialized at three vertical levels within the sampling range of the impactors. The simulations were driven by the Global Data Assimilation System (GDAS) meteorological fields, at 1° × 1° spatial resolution, providing a realistic representation of the synoptic-scale circulation.

To further characterize the origin of the sampled air-masses and to quantify potential source contributions, the FLEXPART-WRF model (Brioude et al., 2013) was employed in backward mode to compute source–receptor relationships. The FLEXPART simulations were driven by hourly WRF-CHEM meteorological fields (Grell et al., 2005) at a horizontal resolution of 20 × 20 km. The model domain is shown in Fig. A1. The resulting emission sensitivity fields (s m^3 kg^{-1}), displayed on a logarithmic scale, indicate regions where surface emissions are most likely to contribute to the observed aerosol population.

To provide an independent observational constraint on the modeled transport pathways and source regions, satellite-based dust products were additionally examined. Specifically, the DUST-RGB product from the Spinning Enhanced Visible and InfraRed Imager (SEVIRI) onboard the Meteosat Second Generation (MSG) satellite and the Atmospheric Infrared Sounder (AIRS) Dust Score derived from measurements aboard the NASA Aqua satellite were used to assess the presence of active dust emissions along the inferred transport routes. The Dust RGB product is a false-colour red–green–blue (RGB) composite based on thermal infrared channels, in which mineral dust is typically depicted by colours ranging from pink to violet, whereas the AIRS Dust Score is derived from differences between radiance measurements in channels sensitive to dust and those not sensitive to dust, where more intense reddish tones indicate increased confidence in the presence of airborne dust.

3. Results

3.1 Atmospheric conditions over the analyzed period

From the 25 cases sampled in June 2022, 14 were selected for detailed analysis, as these corresponded to instances where impactors were opened within the SAL and provided consistent datasets. Their key characteristics, including sampling time, altitude range, AOD and cloud presence, are summarized in Table 2. Additional information on air-masses origin is provided in Table A3.

Table 2. Overview of the in-situ measurement cases. Day, time and height of sampling, aerosol optical depth (AOD), and presence of clouds during the flight.

Impactor identifier	Impactor sampling time (UTC)	Impactor sampling altitude range (m)	AOD from AERONET	Cloud-free (from lidar observations)
A_03	11/6/2022 18:39-18:43	2400-3200	-	no
A_04	11/6/2022 18:45-18:47	1800-2200	-	no

https://doi.org/10.5194/egusphere-2026-921
Preprint. Discussion started: 18 May 2026

A_06	15/6/2022 12:37-12:40	2389-3126	-	-
A_07	15/6/2022 12:41-12:45	1255-2081	-	-
A_08	19/6/2022 18:33-18:36	1550-2399	-	no
A_09	20/6/2022 5:25-5:27	2278-3025	-	no
A_10	17/6/2022 18:15-18:20	2499-3384	-	yes
A_11	26/6/2022 04:27-04:33	3151-4990	>0.3	no
A_12	23/6/2022 18:05-18:10	2097-3139	-	no
A_15	24/6/2022 18:56-19:01	3142-4789	>0.43	yes
A_16	24/6/2022 19:03-19:07	1596-2640	>0.43	yes
A_18	26/6/2022 04:33-04:38	1784-2894	>0.3	no
C_02	28/6/2022 12:33-12:37	2308-3053	>0.6	-
C_05	30/6/2022 04:31-04:36	2079-3126	>0.2	yes

An overview of the 8-day backward trajectories of the sampled air-masses for each case is provided in Fig. A2. The trajectories suggest that aerosols were predominantly mineral dust particles, as meteorological conditions favored the transport of air-masses from mainland Africa toward the Cabo Verde islands, following the SAL pathway, with a few cases indicating origins over the ocean.

These transport patterns, were further supported by ground-based remote sensing observations conducted during the same period over Mindelo. Specifically, the AOD of the atmospheric column, measured from AERONET sun photometer observations (Dubovik et al., 2006; Dubovik & King, 2000), ranged from 0.1 to 0.7, with a mean value of approximately 0.4 at 532 nm (Fig. 2a) and the Angstrom Exponent (AE), calculated between 440 and 675 nm, ranged from 0 to 0.3, with a mean value around 0.1 (Fig. 2b). These AE values are characteristic of coarse-mode particles (Schuster et al., 2006) and are consistent with those reported for desert dust by Toledano et al. (2009) for the area of Morocco. Together with the HYSPLIT-derived air-mass trajectories, the observed optical characteristics of the particles provide strong evidence of mineral dust presence and support the dust-related objectives of the campaign.

(a)

https://doi.org/10.5194/egusphere-2026-921
Preprint. Discussion started: 18 May 2026

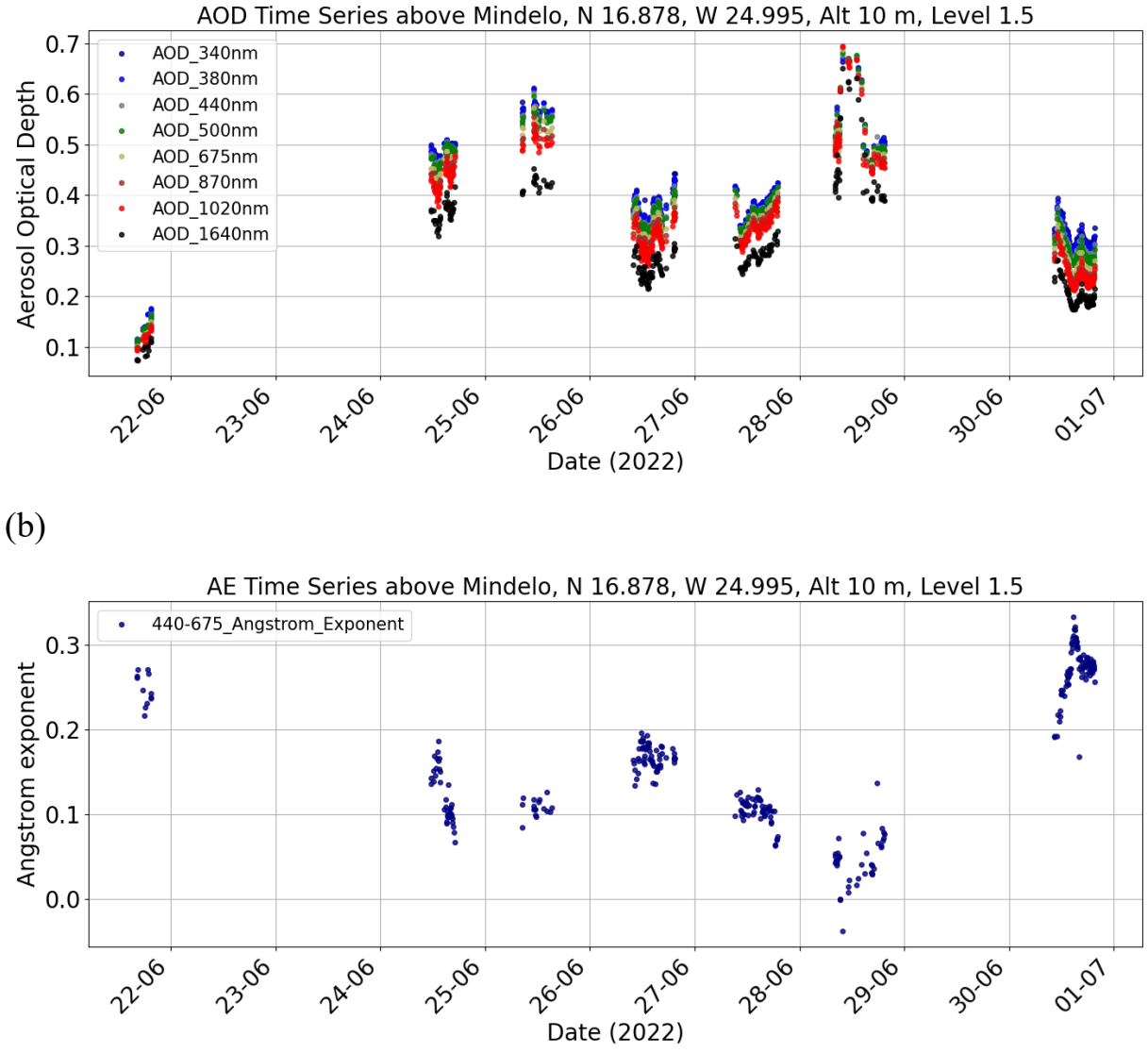

Figure 2. AERONET retrievals of (a) AOD and (b) AE at 440–675 nm, of particles over Mindelo from 21 to 30 June 2022.

Overall, aerosol conditions above Mindelo remained relatively stable throughout the ASKOS campaign. Lidar observations in Mindelo show that typically, the marine boundary layer (MBL) extended up to approximately 1 km in altitude and was overlaid by SAL reaching heights up to 6 km (Tsichla et al., in preparation). The vertical extent of SAL and the desert dust concentration varied across the observation period, offering a diverse range of aerosol scenarios (Fig. 3). Clouds were very frequently observed near the top of MBL, while, on occasion, cloud formation was also detected at the top of SAL, sometimes accompanied by supercooled cloud layers.

https://doi.org/10.5194/egusphere-2026-921
Preprint. Discussion started: 18 May 2026

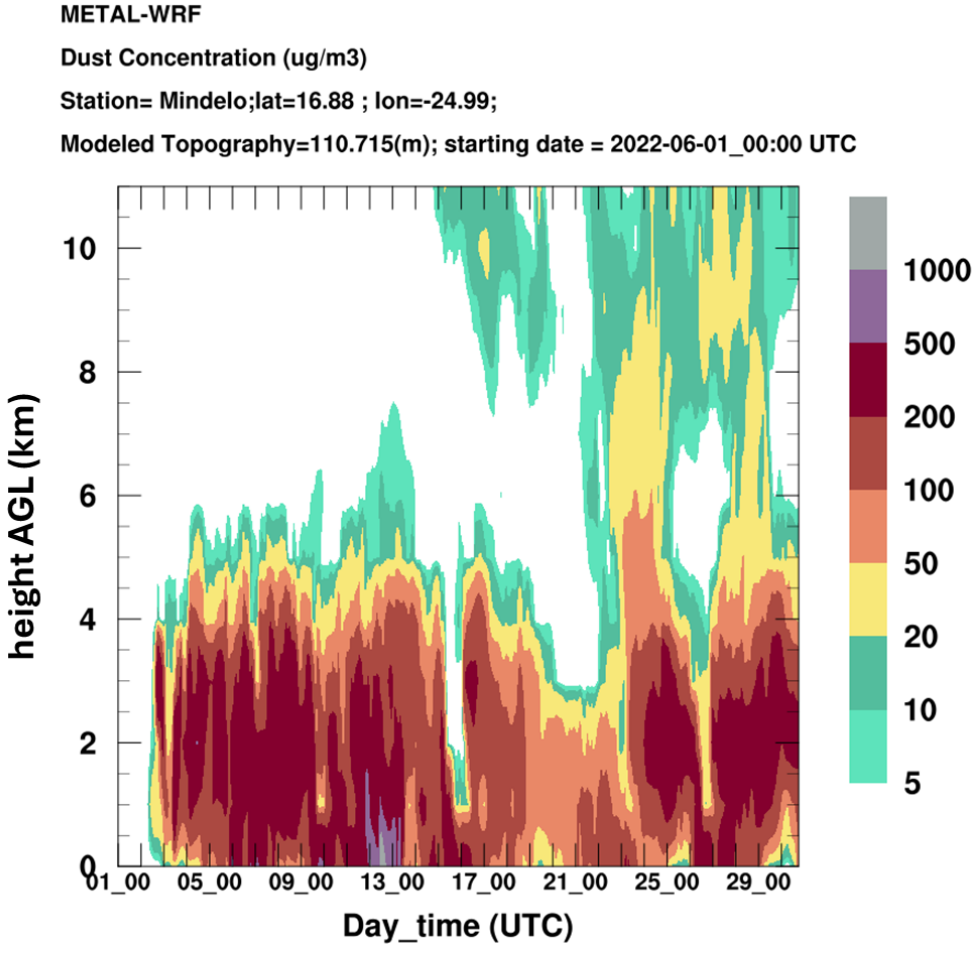

Figure 3. Simulated dust concentration (µg/m3) at the model layers above Mindelo station for the period 1-30 June 2022.

3.2 In-situ observations of the dust particle mineralogical composition

This subsection presents the mineralogical composition of the airborne particles collected in-situ during the UAV flights, as determined by SEM-EDX analysis. The main mineralogical groups observed for each case, are shown in Fig. 4. A particle diameter of 25 µm was adopted as the upper size threshold for inclusion in the analysis, corresponding to the mean upper particle size observed across all cases. Particles larger than this threshold accounted for less than 0.2% of the total particle population in each sample, providing insufficient statistics for a robust mineralogical analysis; their inclusion could therefore introduce disproportionate uncertainty into the inferred composition.

https://doi.org/10.5194/egusphere-2026-921
Preprint. Discussion started: 18 May 2026

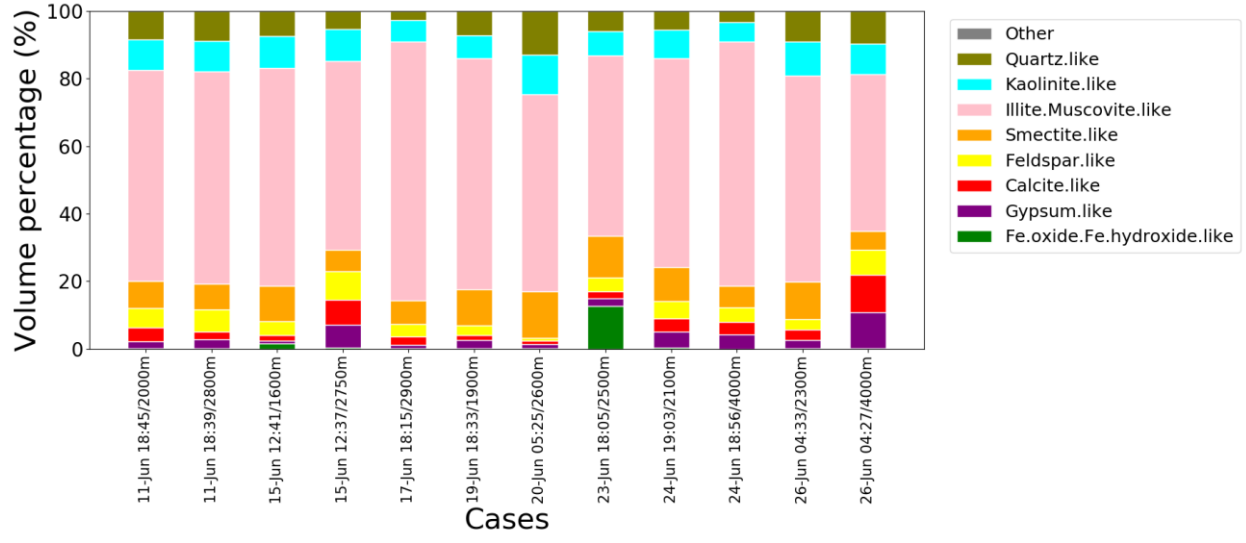

Figure 4. Approximated volume percentages of mineralogical groups of desert dust particles inside the SAL, during the ASKOS campaign.

The average mineralogical composition by volume is dominated by the group of illite/muscovite (62%), followed by smectite (9%), kaolinite (9%), quartz (7%), feldspar (5%), calcite (4%), gypsum (3%) and Fe-oxide/Fe-hydroxide (1%). These results are consistent with previous observations across different sampling altitudes, including free-tropospheric measurements at the Izaña Observatory, Tenerife (2367 m a.s.l.) (Jeong et al., 2016), aircraft observations over Niger up to 1500 m a.s.l. (Chou et al., 2008), near-surface measurements (1.5 m) in the Draa Valley in southeastern Morocco (Panta et al., 2023), and soil samples from multiple locations across North Africa (Li et al., 2024). The dominance of clay minerals, such as illite, smectite and kaolinite, is consistent with long-range transported desert dust from Sahara, as heavier particles tend to settle out while fine silicates and clays (<7.3 μm in diameter) remain suspended in the atmosphere for longer time of periods (Maring et al., 2003). This is supported by the fact that most air-masses during the campaign remained above 2 km altitude for the majority of their trajectories (Fig. A2).

Slightly more distinct mineralogical compositions were observed in the cases of 23 June (sampling at ~2.5 km) and 15 June (sampling at ~1.6 km), which exhibited above-average fractions of Fe-oxide and Fe-hydroxide. The cases of 26 June (sampling at ~4 km) and 15 June (sampling at ~2.7 km), on the other hand, showed enhanced contributions of calcite and gypsum relative to the average. The discussion is therefore structured according to these contrasting mineralogical signatures.

The 23 June case sampled air-masses within the SAL between 2.1 and 3.1 km altitude and exhibited the highest fraction of Fe-oxide/Fe-hydroxide (12%) among all analyzed samples. HYSPLIT backward trajectories and FLEXPART source–receptor sensitivity analyses (Fig. 5a–c) indicate that the air-masses observed above Mindelo at 18:00 UTC originated from East Africa and the Upper Guinea region.

Dust RGB and Dust Score satellite imagery (Fig. 5d–g) reveal active dust emissions along the inferred transport pathways. On 18 June, the violet coloration on the Dust RGB observations (Fig. 5d; red circle) show dust presence over Liberia and Côte

https://doi.org/10.5194/egusphere-2026-921
Preprint. Discussion started: 18 May 2026

d'Ivoire, coinciding with the period during which the air-mass resided near the surface over this region according to both transport models. Subsequent imagery on 19–21 June indicates continued dust activity over southern Mali along the HYSPLIT-derived pathways.

250 These regions lie along the northern margin of the Upper Guinea tropical rainforest zone, which extends from Guinea and Sierra Leone in the west through Liberia, Côte d'Ivoire, and Ghana to Togo in the east (Fig. 5h; red circle). The elevated Fe-oxide/Fe-hydroxide fractions observed in this case are consistent with the mineralogical soil iron distribution reported by (Solomos et al., 2023), which identifies enhanced iron concentrations across the Upper Guinea region (Fig. 5i).

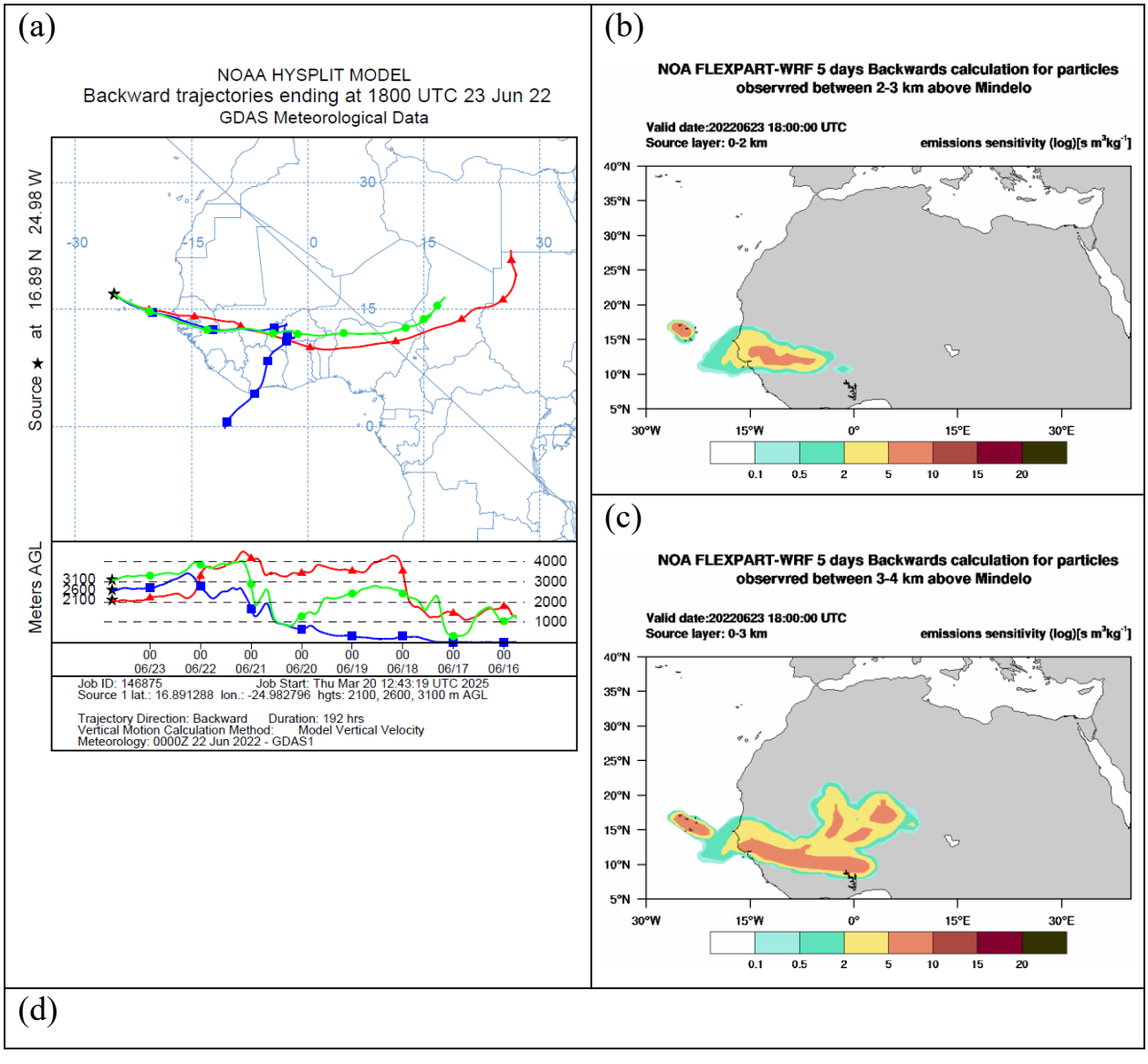

https://doi.org/10.5194/egusphere-2026-921
Preprint. Discussion started: 18 May 2026

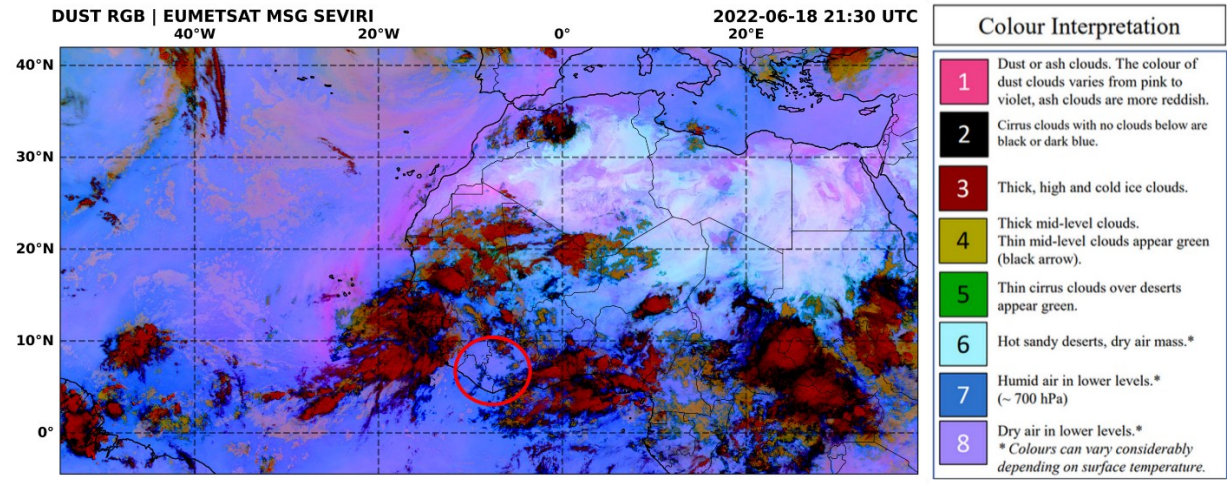

(e)

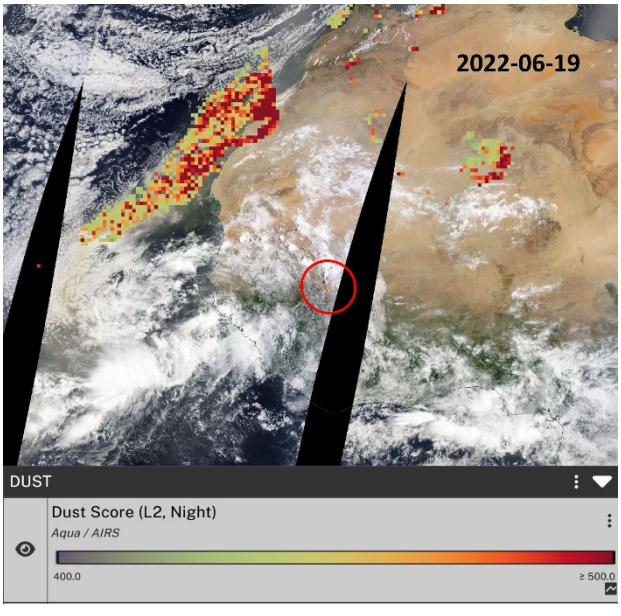

(f)

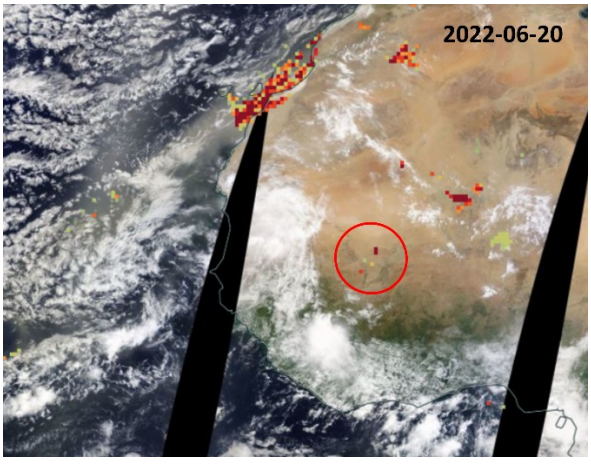

(g)

https://doi.org/10.5194/egusphere-2026-921
Preprint. Discussion started: 18 May 2026

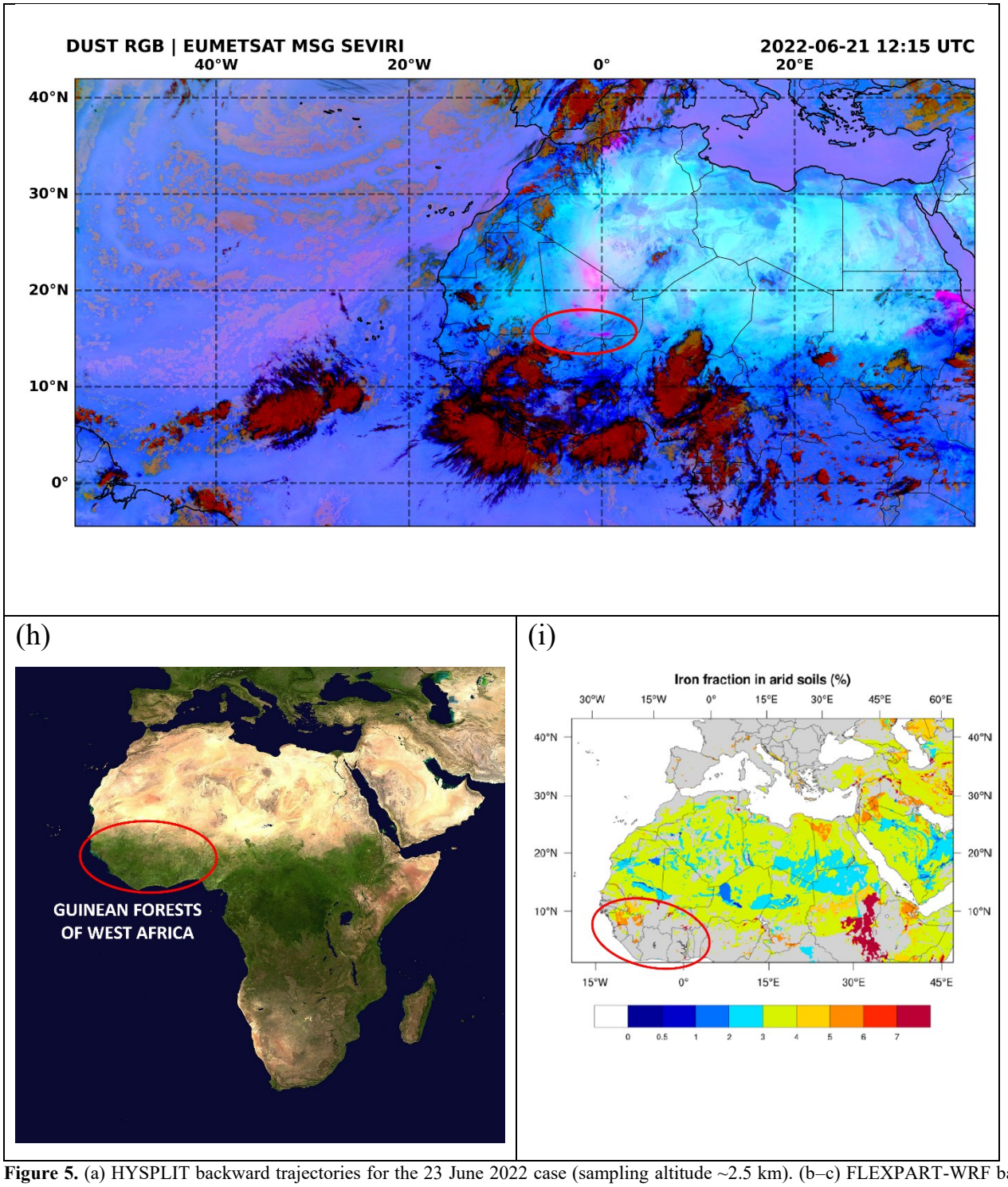

Figure 5. (a) HYSPLIT backward trajectories for the 23 June 2022 case (sampling altitude ~2.5 km). (b–c) FLEXPART-WRF backward emission sensitivity fields for particles observed between 2–3 km and 3–4 km above Mindelo, respectively. (d) MSG–SEVIRI Dust RGB composite for 18 June 2022 (source: EUMETSAT). (e–f) AIRS Dust Score (day and night) for 19 and 20 June 2022, respectively, overlaid

https://doi.org/10.5194/egusphere-2026-921
Preprint. Discussion started: 18 May 2026

on MODIS corrected reflectance (source: GES DISC). (g) MSG–SEVIRI Dust RGB composite for 21 June 2022. In panels (d–g), red circles indicate the trajectory crossing over the inferred source region. (h) Satellite image of the Upper Guinea tropical rainforest region (source: NASA Earth Observatory). (i) Mineralogical soil iron distribution over arid and semi-arid regions of North Africa (source: Solomos et al. (2023)), with the Upper Guinea region highlighted.

The second-highest fraction of Fe-oxide/Fe-hydroxide (1.5%) was observed on 15 June, when air-masses were sampled within the SAL at altitudes between 1.3 and 2.1 km. This case exhibited a transport pattern similar to that identified for 23 June. Backward trajectory and dispersion analyses (Fig. 6a–b) indicate that the sampled air-masses originated from northwestern Africa and the Upper Guinea region.

Dust RGB observations on 8, 9, and 12 June (Fig. 6c, e, g), together with the corresponding Dust Score imagery (Fig. 6d, f, h), reveal active dust emissions along the primary HYSPLIT transport pathway (Fig. 6a; blue line), centered near ~25° N and ~0° E in the Mali–Algeria border region. Emissions were strongest on 8 and 9 June, while weaker but still detectable emissions occurred on 12 June.

Dust activity along the secondary HYSPLIT pathway (Fig. 6a; green line) was less pronounced (Fig. 6c, e, g) but should not be neglected, as dust production in tropical and semi-vegetated regions is typically weaker than in arid source areas. Transport over these regions may nevertheless have contributed to the observed Fe-oxide/Fe-hydroxide fraction, suggesting the influence of oxidative and convective processing over tropical forested environments.

Identifying potential source regions of Fe-oxide/Fe-hydroxide–rich minerals, such as hematite, is particularly relevant for radiative studies, given their strong influence on dust absorption (Li et al., 2024), as well as for ocean biogeochemistry through the role of iron as a limiting micronutrient for phytoplankton (Martin & Fitzwater, 1988).

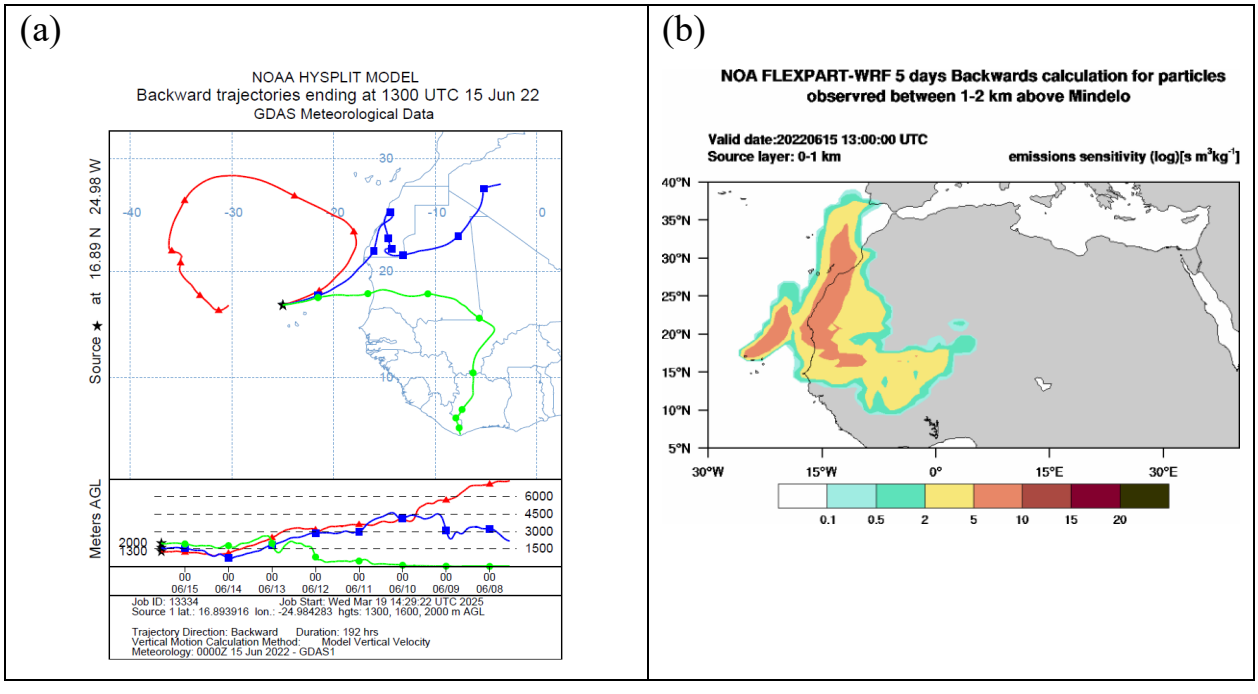

https://doi.org/10.5194/egusphere-2026-921
Preprint. Discussion started: 18 May 2026

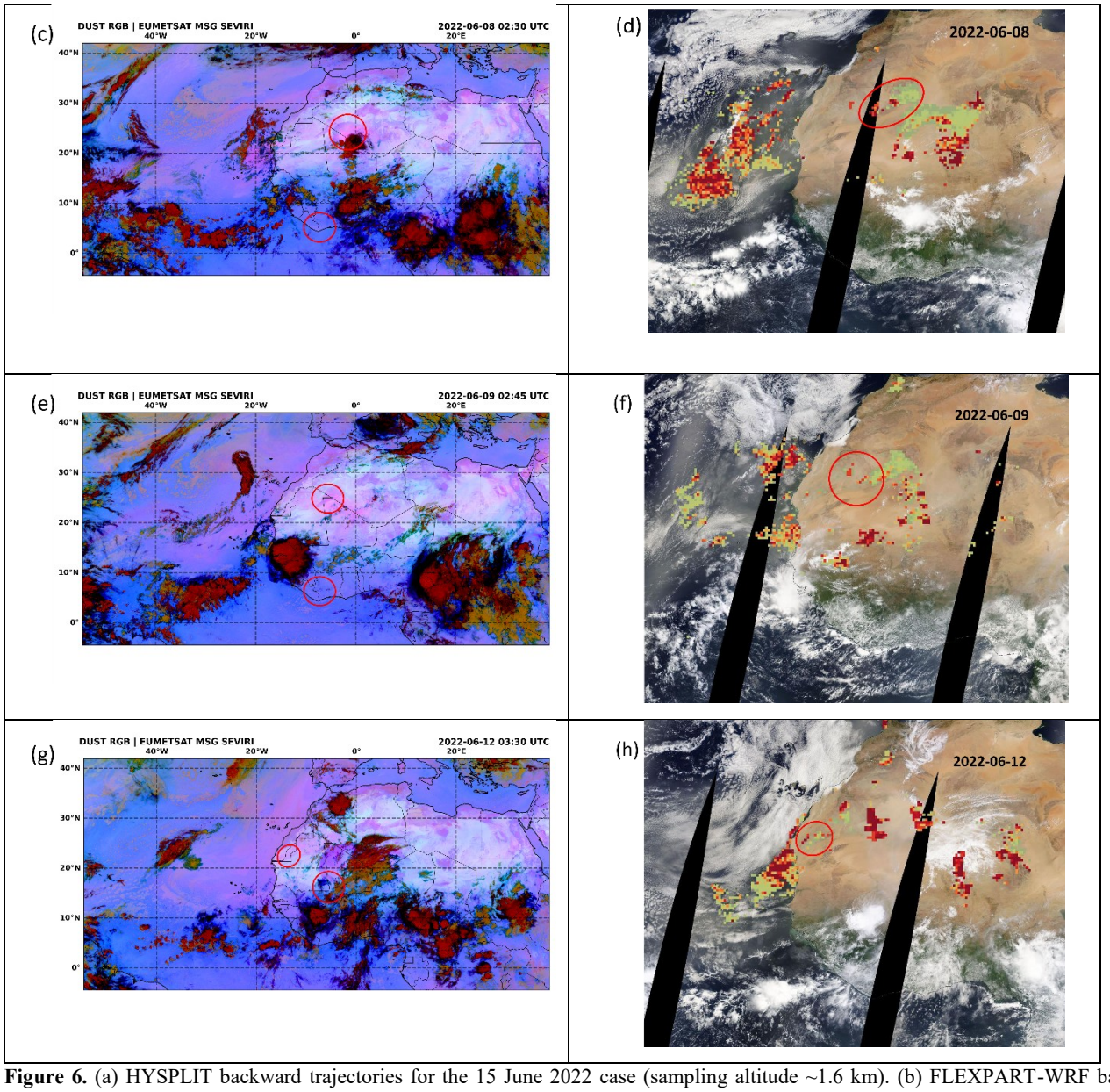

Figure 6. (a) HYSPLIT backward trajectories for the 15 June 2022 case (sampling altitude ~1.6 km). (b) FLEXPART-WRF backward emission sensitivity fields for particles observed between 1–2 km above Mindelo. (c, e, g) MSG–SEVIRI Dust RGB composites for 8, 9, and 12 June 2022, respectively (source: EUMETSAT). (d, f, h) AIRS Dust Score imagery for the corresponding dates, overlaid on MODIS/VIIRS corrected reflectance (source: GES DISC). In panels (c–h), red circles indicate the trajectory crossing over the inferred source regions.

The remaining cases exhibiting distinct mineralogical compositions are characterized by enhanced calcite and gypsum fractions. One such case is the second sampling on 15 June, which collected air-masses within SAL between 2.4 and 3.1 km altitude and exhibited the second-highest fractions of calcite (7%) and gypsum (7%).

https://doi.org/10.5194/egusphere-2026-921
Preprint. Discussion started: 18 May 2026

HYSPLIT backward trajectories indicate that the sampled air-masses originated over central Africa and traversed through Nigeria, Mali, and Mauritania before reaching Cabo Verde on 15 June at 13:00 UTC (Fig. 7a). FLEXPART backward emission sensitivity fields for the 2–3 km and 3–4 km layers (Fig. 7b–c) further highlight enhanced source–receptor sensitivity over northwestern Africa, particularly over Mauritania and Western Sahara.

Dust RGB observations on 11–13 June, together with corresponding Dust Score imagery (Fig. 7d–i), reveal persistent dust emissions along the inferred transport pathways over Mali, Mauritania, Algeria, Western Sahara, and Morocco. The elevated calcite and gypsum fractions observed in this case are consistent with the mineralogical characteristics of these source regions, which are known to be rich in calcite- and gypsum-bearing soils, as indicated by mineralogical maps (Fig. 7j–k).

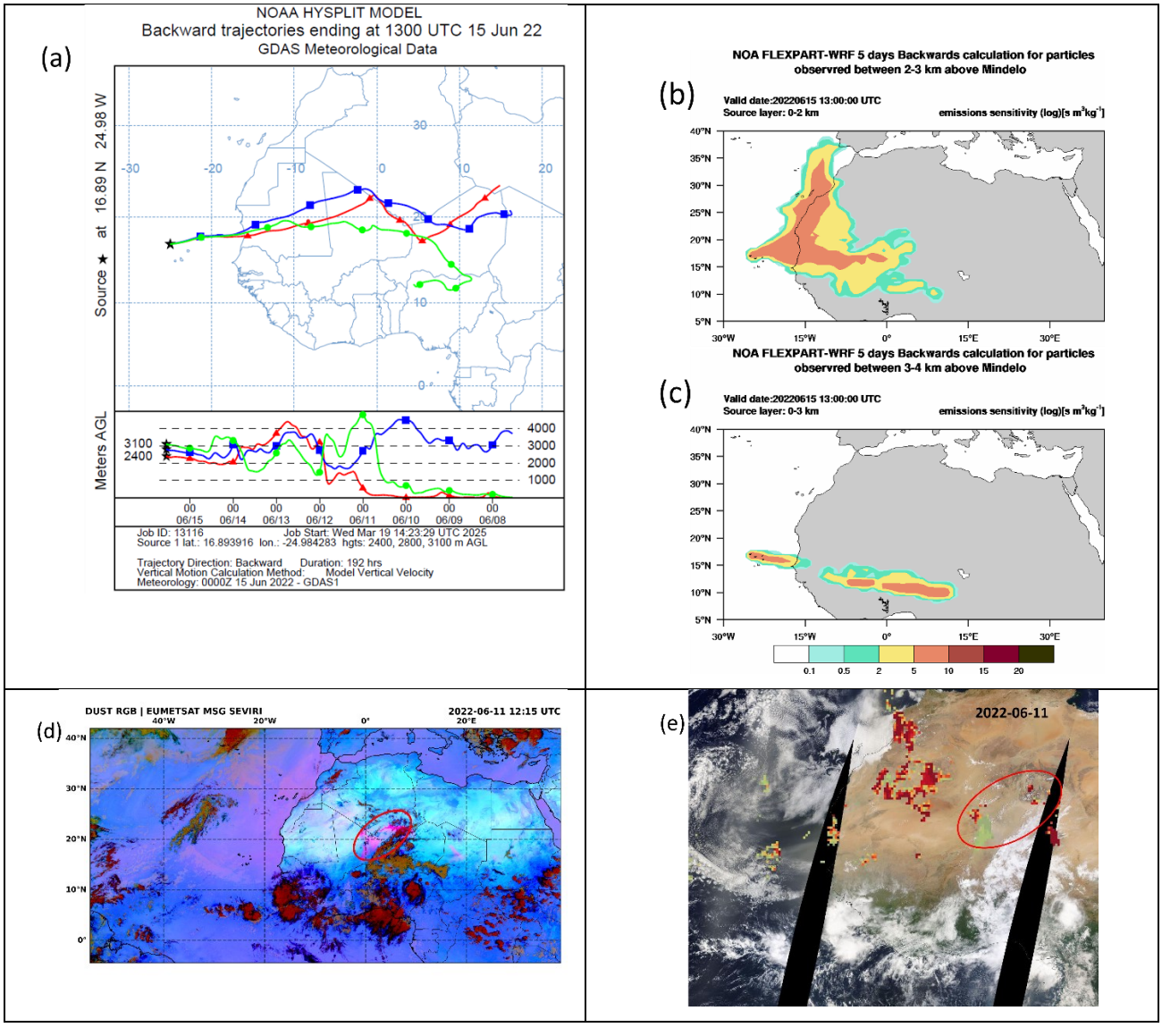

https://doi.org/10.5194/egusphere-2026-921
Preprint. Discussion started: 18 May 2026

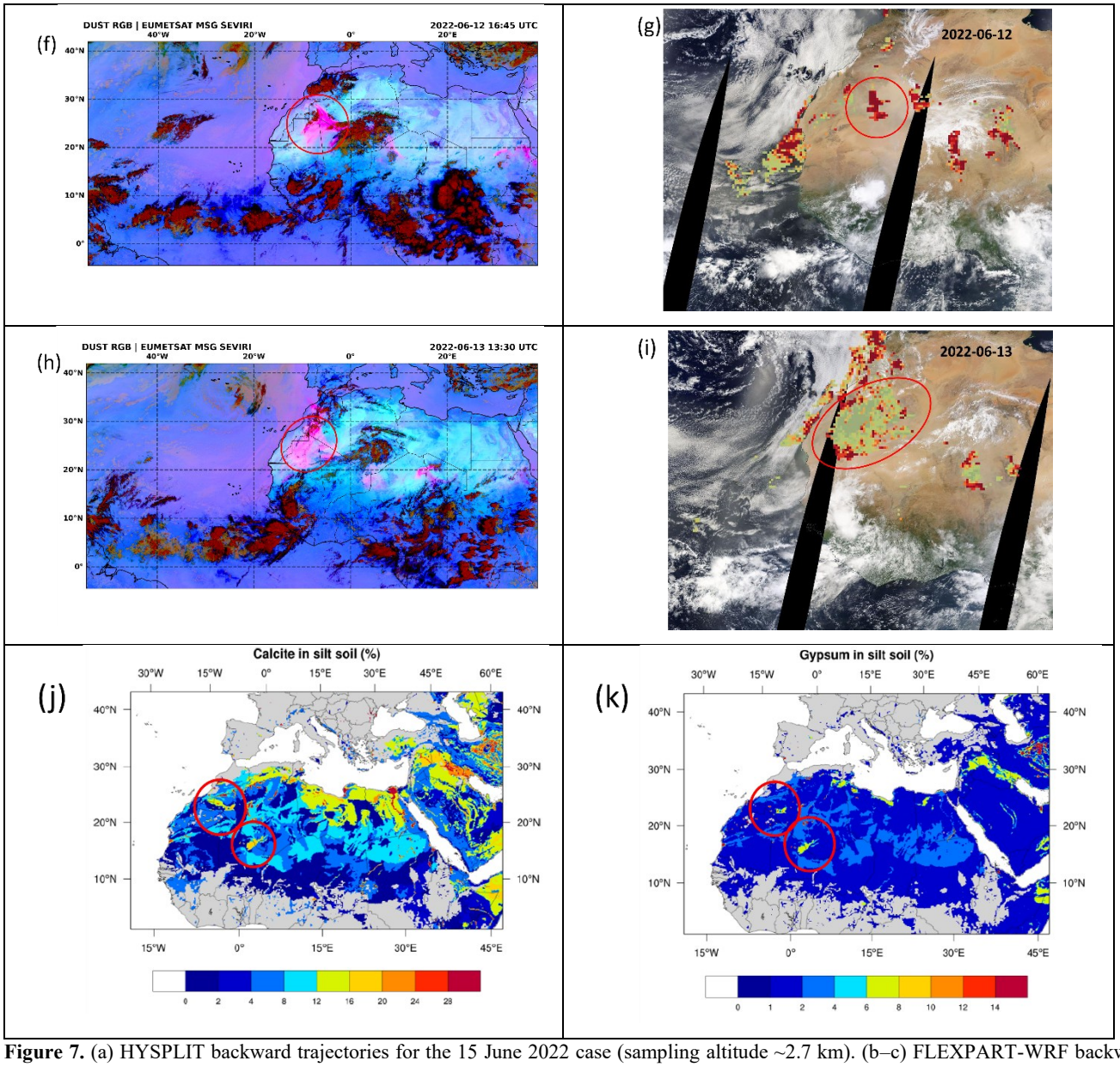

Figure 7. (a) HYSPLIT backward trajectories for the 15 June 2022 case (sampling altitude ~2.7 km). (b–c) FLEXPART-WRF backward emission sensitivity fields for particles observed between 2–3 km and 3–4 km above Mindelo, respectively. (d, f, h) MSG–SEVIRI Dust RGB composites for 11, 12, and 13 June 2022, respectively (source: EUMETSAT). (e, g, i) AIRS Dust Score imagery for the corresponding dates, overlaid on MODIS/VIIRS corrected reflectance (source: GES DISC). In panels (d–i), red circles indicate the trajectory crossing over the inferred source regions. (j–k) Mineralogical soil calcite and gypsum distribution maps for arid and semi-arid regions of North Africa (source: Solomos et al. (2023)), with the northeastern Mali and western Algeria region highlighted.

Finally, the 26 June case sampled air-masses within SAL, between 3.1 and 5.0 km altitude, and exhibited the highest fractions of calcite (11%) and gypsum (11%) among all analyzed samples. HYSPLIT backward trajectories indicate that the air-masses originated over eastern Africa and remained predominantly above ~3 km during the final 8 days prior to arrival over Cabo

https://doi.org/10.5194/egusphere-2026-921
Preprint. Discussion started: 18 May 2026

Verde on 26 June at 05:00 UTC (Fig. 8a), suggesting dust incorporation through long-range transport and/or vertical mixing from lower altitudes.

Dust RGB observations on 20, 23 and 25 June, together with corresponding Dust Score imagery (Fig. 8b–g), reveal dust emissions along the inferred transport pathways over eastern Sudan, the region between Mali and Nigeria, and most prominently over Mali (Fig. 8f-g).

The elevated calcite and gypsum fractions observed in this case are consistent with the mineralogical characteristics of the Mali region, as indicated by the mineralogical maps presented in Fig. 7j–k.

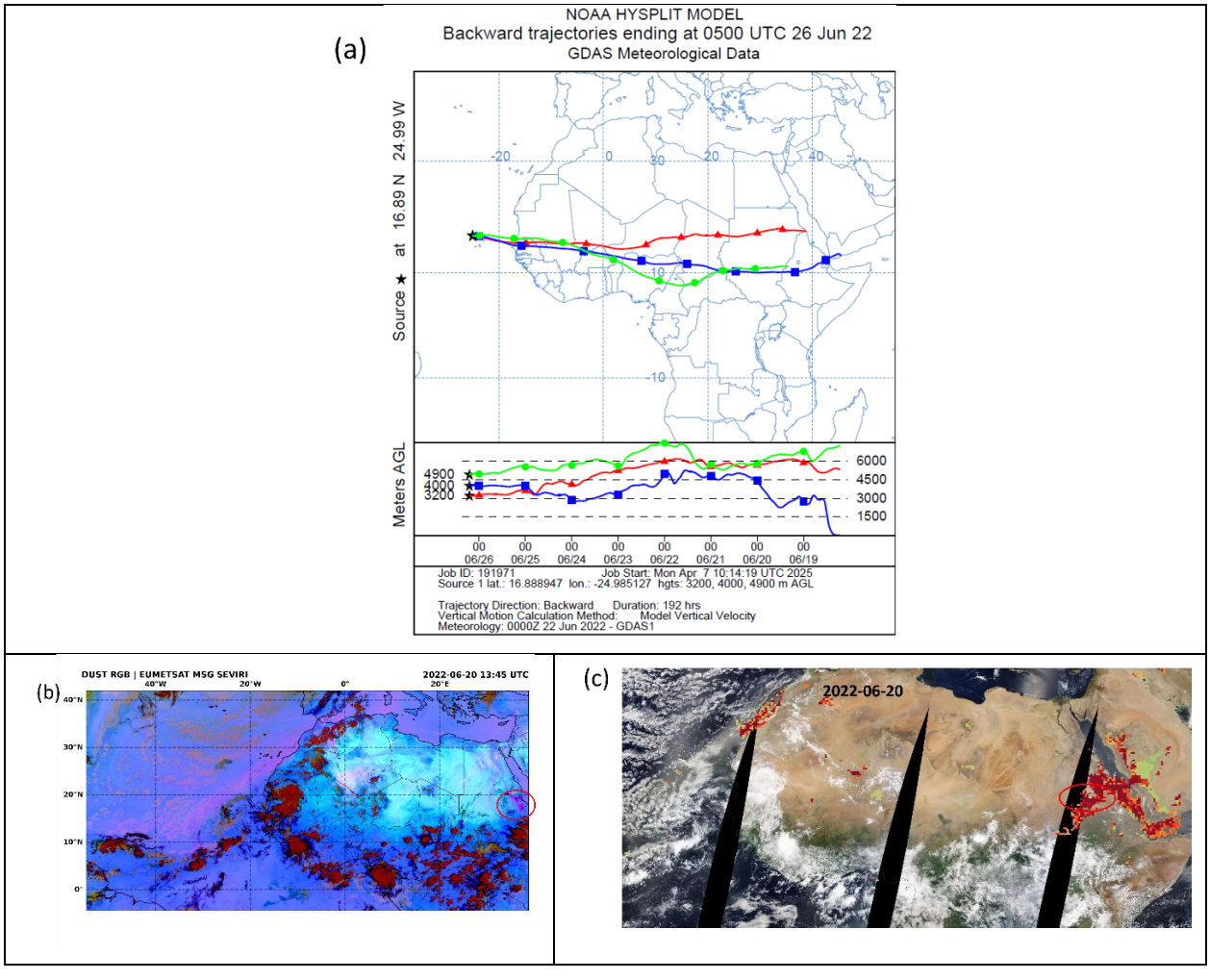

https://doi.org/10.5194/egusphere-2026-921
Preprint. Discussion started: 18 May 2026

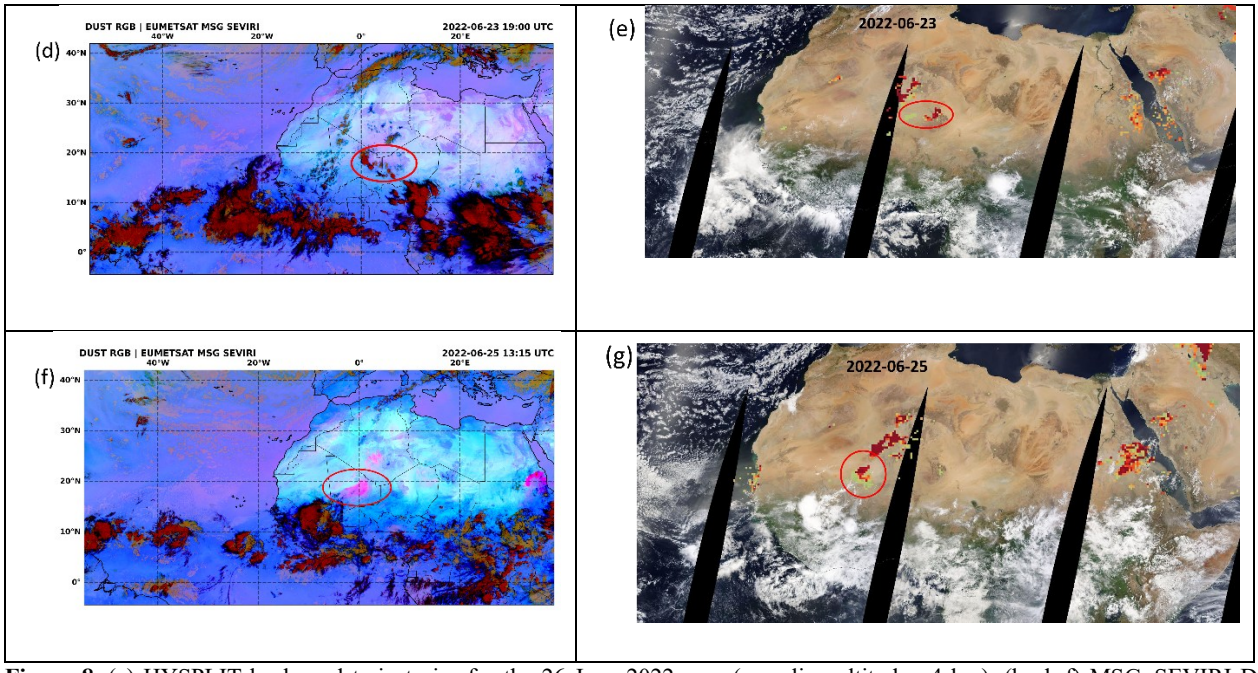

Figure 8. (a) HYSPLIT backward trajectories for the 26 June 2022 case (sampling altitude ~4 km). (b, d, f) MSG–SEVIRI Dust RGB composites for 20, 23, and 25 June 2022, respectively (source: EUMETSAT). (c, e, g) AIRS Dust Score imagery for the corresponding dates, overlaid on MODIS/VIIRS corrected reflectance (source: GES DISC). In panels (b–g), red circles indicate the trajectory crossing over the inferred source regions.

Taken together, these findings demonstrate that the commonly assumed vertical homogeneity of mineral dust composition within a given day or hour does not always hold. Instead, vertical variability can arise when different atmospheric layers are influenced by air-masses originating from distinct African source regions, as observed on 15 June. In particular, within the cases examined in this study, air-masses advected over arid soil regions were associated with enhanced Ca-rich particles (Claquin et al., 1999; Desboeufs & Cautenet, 2005), whereas transport over tropical forested regions was linked to elevated proportions of Fe-oxide/Fe-hydroxide–like particles, likely reflecting enhanced oxidation and atmospheric processing (Lelieveld et al., 2008; Tripathi et al., 2025).

3.3 Comparison of in-situ measurements, AERONET, and METAL-WRF model

3.3.1 Total columnar mass from AERONET observations and from METAL-WRF

First, a comparison of the total columnar mass is performed to assess how well the METAL-WRF model reproduces the magnitude of the aerosol load. For this purpose, we use the AERONET product of column-integrated aerosol volume, which can be converted to a columnar mass by assuming a representative particle density. As demonstrated in the previous section, the atmospheric column during the examined cases is dominated by desert dust particles; therefore, the derived aerosol mass can be considered a first-order approximation of the dust load, which is what METAL-WRF model provides.

https://doi.org/10.5194/egusphere-2026-921
Preprint. Discussion started: 18 May 2026

330 To better understand the model's performance, mass values are provided for each hour within a +/-3-hour window centered on the sun-photometer observations, to identify potential time shifts in the peak correlation between simulations and measurements (Fig. 9).

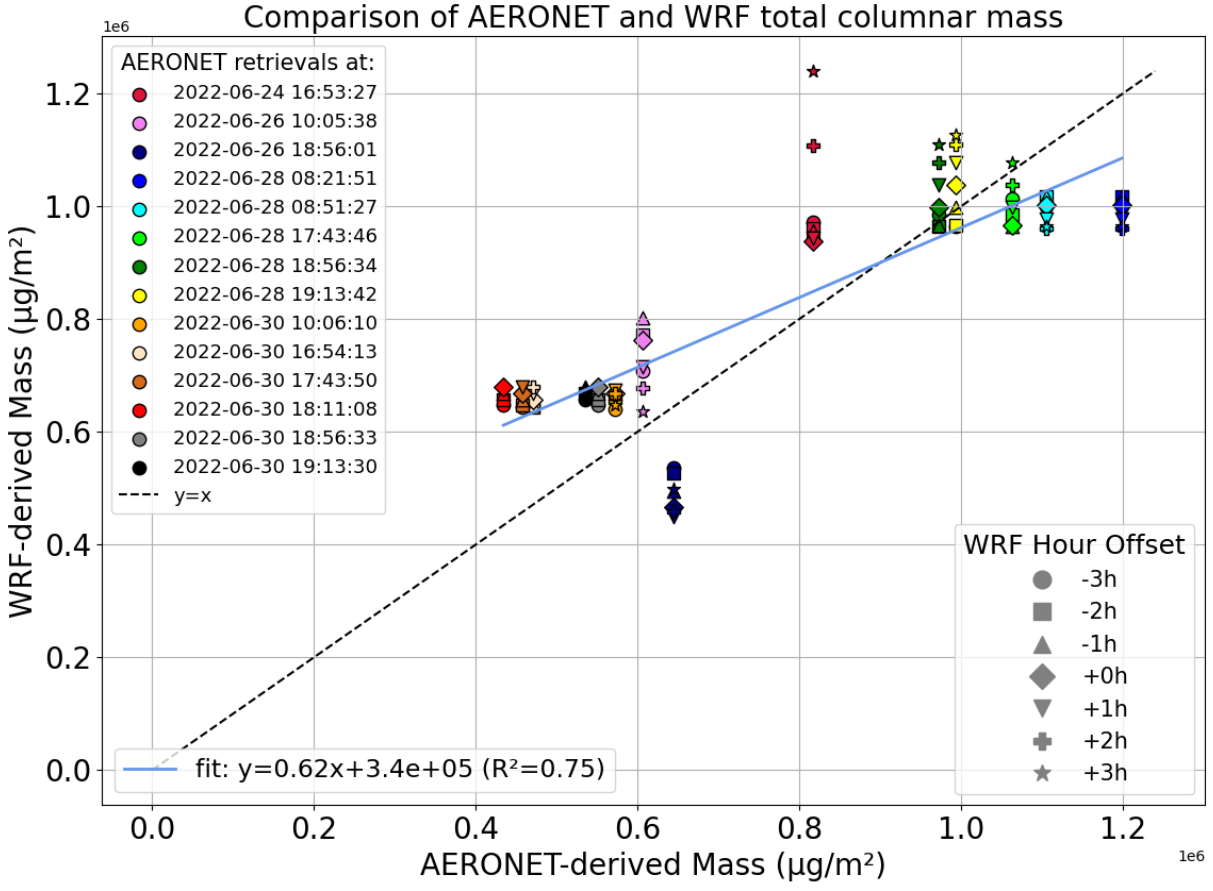

335 **Figure 9.** Comparison of total columnar mass retrieved from sun-photometer measurements provided by AERONET site in Mindelo and the METAL-WRF model. Model values correspond to a 6-hour window centered on the AERONET measurement to account for temporal variability.

A general good agreement is observed between METAL-WRF-derived dust mass and AERONET measurements, with a regression slope of 0.62 and a correlation coefficient of 0.87. The model often reproduces the observed values ahead of time, 340 although in some cases the best correspondence occurs later. To account for this temporal variability, the model-derived elemental mass concentrations presented in the following subsection are averaged over a 6-hour window centered on the in-situ measurements, with the corresponding standard error calculated to represent the uncertainty of the mean within this interval.

https://doi.org/10.5194/egusphere-2026-921
Preprint. Discussion started: 18 May 2026

3.3.2 Elemental mass percentages comparison from in-situ measurements and METAL-WRF model

The comparison focuses on elemental mass percentages rather than absolute concentrations, due to the inherent limitations of the SEM/EDX technique used for the analysis of the in-situ samples, in quantifying absolute values accurately (Newbury & Ritchie, 2011). Figure 10 shows the in-situ and METAL-WRF mean mass percentages of Si, Fe, Ca, Al and S for the full observation period from 11 to 30 June 2022.

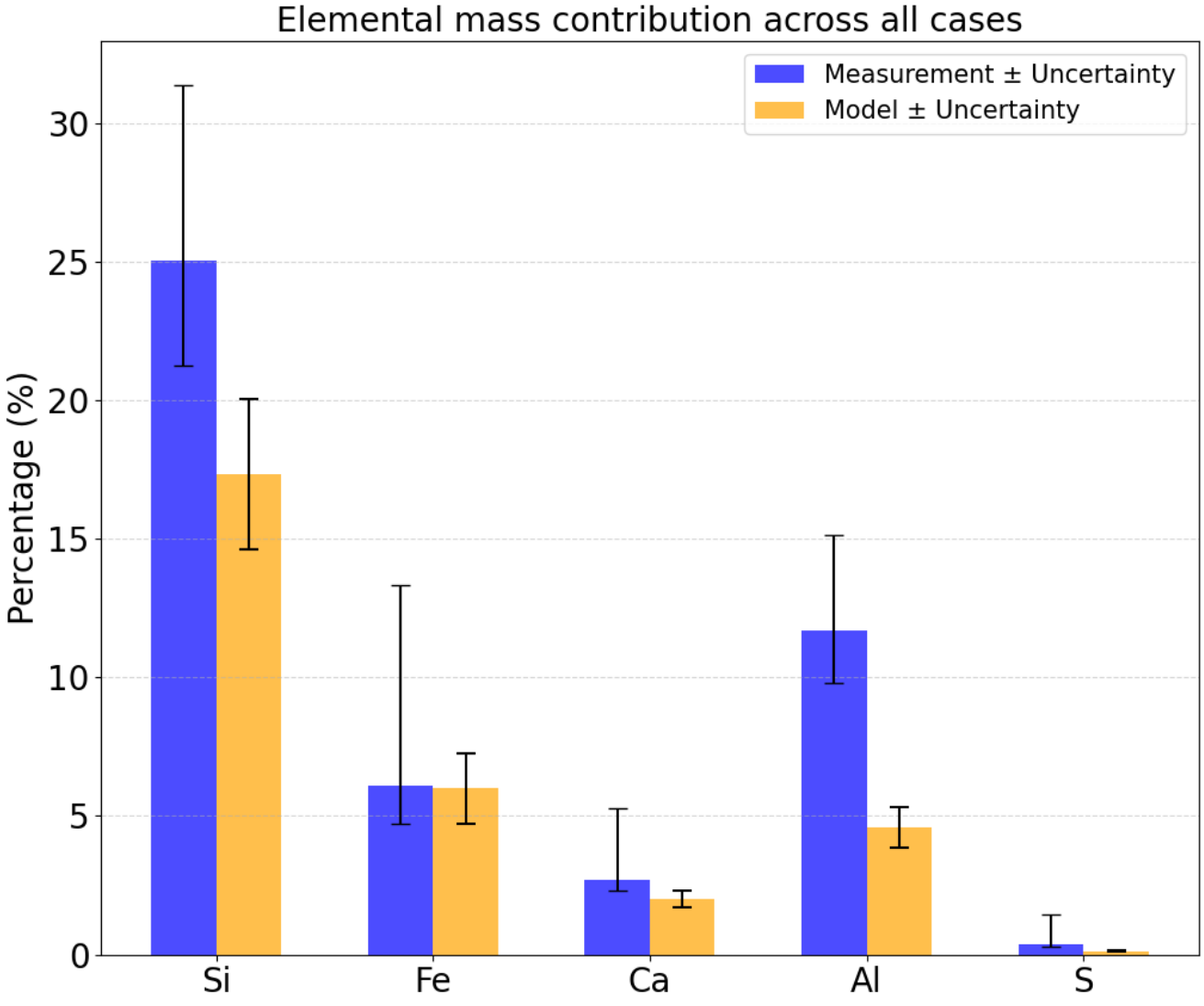

Figure 10. In-situ measurements and METAL-WRF model-derived averaged mass percentages of Si, Fe, Ca, Al, and S over the full observation period (11–30 June 2022).

Based on the measurements, Si is the dominant dust component, accounting for approximately 25% (21-31%) of the total mass, followed by Al at ~12% (10-15%), Fe at ~6% (5-13%), Ca at ~2.7% (2.3-5.3%), and S at ~0.4% (0.3-1.5%). The

https://doi.org/10.5194/egusphere-2026-921
Preprint. Discussion started: 18 May 2026

corresponding METAL-WRF fractions are ~17±3% for Si, ~4.6±0.7% for Al, ~6±1.3% for Fe, ~2±0.3% for Ca, and ~0.13±0.02% for S. The results indicate that the METAL-WRF model reproduces the mean relative abundances of Fe and Ca, averaged over the 20-day period, within the measurement uncertainty. In contrast, the relative abundances of Si, Al, and S are not well captured by the model, with the largest discrepancy observed for Al.

Previous studies on the measured elemental composition of desert dust particles have reported the following values. Pérez García-Pando et al. (2016) reported 19–21% Si, 7–8% Al, 4% Fe, and 3.5–7% Ca, based on monthly averages from 2002 to 2010 at the Izaña Observatory in Tenerife. Rodriguez-Navarro et al. (2018) reported 24.05% Si, 6.62% Al, 3.69% Fe, 5.72% Ca, and trace amounts of S from 24-hour sampling conducted on 21–23 February 2017 in the urban area of Granada. Solomos et al. (2023) reported comparable elemental concentrations based on monthly averages for August 2017 at the Izaña Observatory.

These percentages are close to those observed in the present study, with marginally higher values reported here. This difference can be attributed to the different sampling altitudes, as previous samples were collected mainly at the surface (e.g., at the Izaña Observatory at ~2.3 km a.s.l.), whereas the current dataset is derived from in-situ UAV sampling spanning ~1.5–5.0 km, thereby capturing vertical variability and reducing near-surface dilution and mixing (Gogoi et al., 2020). Finally, earlier campaigns were conducted in Tenerife and urban Granada, whereas this study was carried out at São Vicente Island, Cabo Verde, where different air masses are generally expected, including urban and sea-salt influences, along with atmospheric aging.

Following the comparison over the entire observation period, a case-by-case comparison is performed for Si, Fe, and Ca. Si is included due to its dominant contribution to the dust mass, whereas Fe and Ca are examined because they exhibit good agreement between model and observations. This event-based analysis enables assessment of the variability in the model's performance across individual cases (Fig. 11).

https://doi.org/10.5194/egusphere-2026-921
Preprint. Discussion started: 18 May 2026

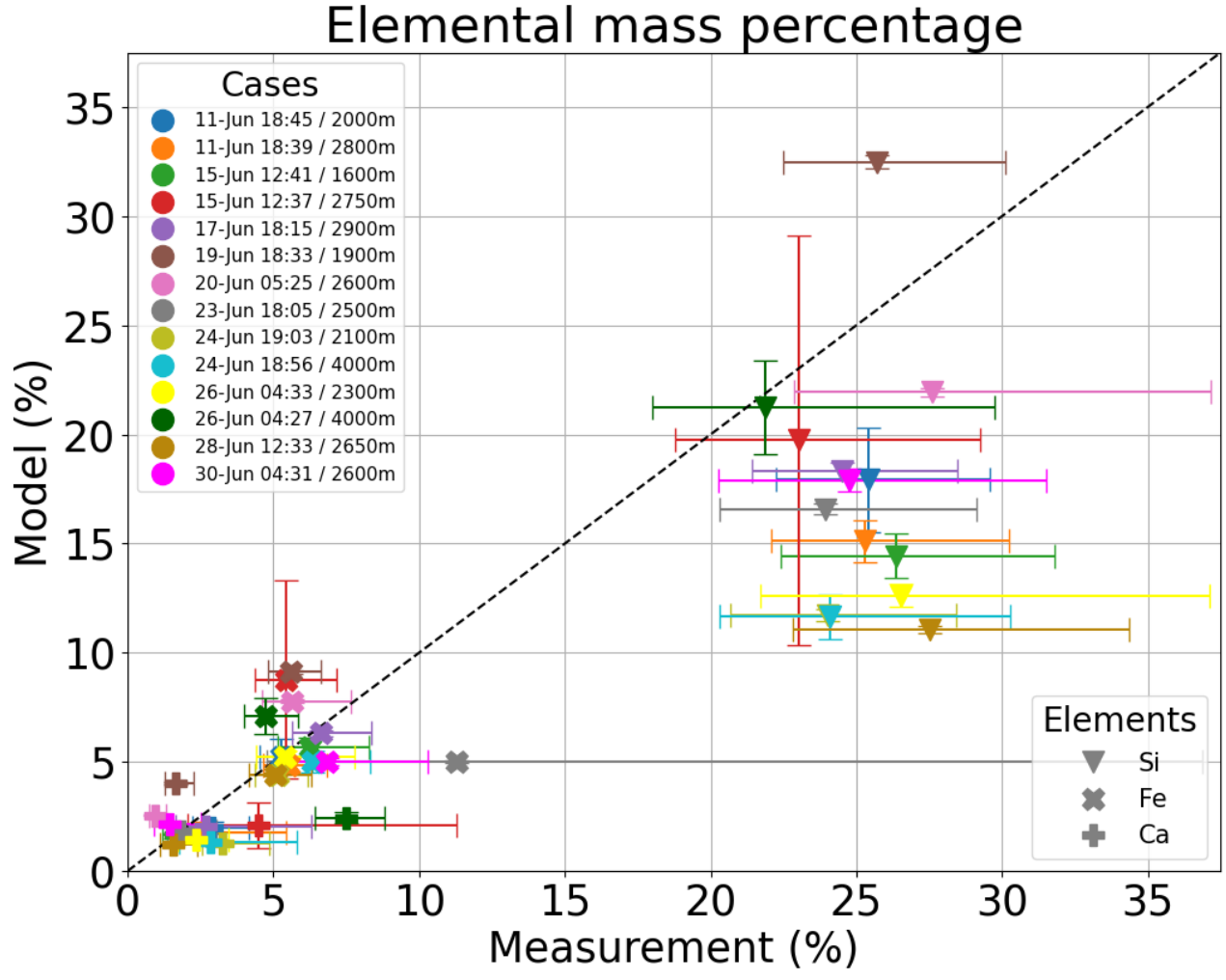

Figure 11. Scatter plot of in-situ measurements versus METAL-WRF model-derived elemental mass percentages for selected elements across all individual cases. Each case is labelled with the measurement time (June 2022, UTC), and the midpoint of the impactor sampling height range.

The linear regression analysis (Fig. A3) shows slopes range from −0.19 to 0.0 with correlation coefficients of 0.2 and 0.0 for Fe and Ca, respectively, while Si exhibits a slope of −0.31 and a correlation coefficient of 0.1. These values indicate that the observed variability from case to case is not well captured by the model.

Such behavior is commonly reported in modeling studies (Shaw, 2008; Yasar et al., 2020), where model outputs averaged over monthly or longer periods tend to show improved agreement with observations compared to higher time-resolution or case-by-case comparisons. This improvement is generally attributed to the smoothing of short-term discrepancies arising from uncertainties in model dynamics, transport processes, and the temporal variability of desert dust composition.

Although the model does not reproduce the observed variability across individual cases, agreement assessed on a case-by-case basis within uncertainty ranges reveals element-dependent behavior. For some elements, the modeled uncertainty range largely

https://doi.org/10.5194/egusphere-2026-921
Preprint. Discussion started: 18 May 2026

overlaps with that of the measurements, whereas for others a systematic deviation is evident. Figure A4 of the Appendix illustrates the temporal evolution of in-situ and model-derived elemental mass percentages for Fe and Al, selected as representative examples of these contrasting behaviors. Fe exhibits consistently good agreement, characterized by overlapping measurement and model uncertainty ranges, whereas for Al no overlap between the two uncertainty ranges is observed.

The Fe/Al ratio derived from the measurements has an average value of 0.52, which nicely agrees with the values reported in previous studies by Formenti et al. (2003) and Kandler et al. (2007), who found ratios of 0.53 and 0.58, respectively. On the other hand, the METAL-WRF model yields a substantially higher ratio of 1.3, suggesting an underestimation of Al, given that Fe aligns well with the measurements. While Fe is a prognostic variable in the model, Al is calculated indirectly based on the concentrations of the modeled minerals (Pérez García-Pando et al., 2016; Solomos et al., 2023). Therefore, certain limitations at the mineralogical source maps and the possible absence of Al containing minerals, may lead to such underestimations.

In contrast, the strong agreement for Fe across all cases is particularly noteworthy given its key role in ocean productivity and radiative processes (Di Biagio et al., 2019; Jickells et al., 2005; N. Mahowald et al., 2011), highlighting the importance of accurate elemental representation in desert dust models for both climate and biogeochemical cycle applications.

4 Conclusions

This study investigates the mineralogical and elemental composition of desert dust during its atmospheric transport at different altitudes above Cabo Verde, as observed during the ASKOS ESA campaign. To this end, in-situ measurements obtained with UAV-mounted impactors were used and compared with corresponding simulations from the METAL-WRF model, of the elemental mass concentrations of key chemical elements (Si, Fe, Ca, Al, and S).

The overall dust mineralogical composition was dominated by clay minerals, with illite/muscovite as the most abundant group, followed by smectite and kaolinite. Quartz, feldspar, calcite, gypsum, and Fe-oxide/Fe-hydroxide were present in smaller proportions. Distinct mineralogical signatures were identified depending on air-mass origin: cases associated with emission activity in northern and central Africa, primarily northern Mali, exhibited enhanced contributions of calcite components, whereas cases linked to air-masses originating from southern Mali, along the northern margin of the Upper Guinea tropical forest zone, showed notable proportions of Fe-oxide and Fe-hydroxide.

This study further compares elemental mass percentages derived from in-situ measurements at multiple atmospheric altitudes with corresponding outputs from the METAL-WRF model, to assess the model's ability to represent key dust components. While good agreement is obtained for Fe and Ca when the elemental mass percentages are averaged over the full observation period, no statistically correlation is found on a case-by-case basis. This indicates that the METAL-WRF model is better suited for climatological-scale applications, such as the assessment of dust radiative forcing or seasonal deposition of mineral dust elements, rather than for day-to-day (weather-scale) predictions. Nevertheless, Fe exhibits overlapping uncertainty ranges between modeled and measured values for almost all cases, a result that is particularly important for studies focusing on ocean biogeochemistry and dust-related radiative processes.

https://doi.org/10.5194/egusphere-2026-921
Preprint. Discussion started: 18 May 2026

These results reflect aspects of the model formulation, as Fe is explicitly represented in the model, with associated uncertainties primarily linked to source-related processes, whereas the remaining elements are inferred indirectly from a limited set of mineral species and their empirical formulas. The observed underestimations are therefore likely related to the absence of certain minerals, such as chlorite, goethite, and vermiculite, in the current mineralogical dataset. In addition, the model lacks detailed information on specific dust source regions, as well as on the seasonality and regional variability of arid and agricultural soil compositions.

These limitations could be addressed by incorporating satellite-based observations of dust source mineralogy, such as those provided by the Earth Surface Mineral Dust Source Investigation (EMIT) imaging spectrometer. The integration of EMIT-derived mineralogical information is planned as part of the future development of this work.

Finally, several sources of uncertainty inherent to both the observational and modeling approaches should be considered when interpreting the findings of this study. On the observational side, factors such as the collection efficiency of the impactors, particle storage and preservation (particularly for sulfate-bearing phases), the morphological determination of sampled particles, and assumptions regarding elemental oxide forms may influence the derived elemental and mineralogical composition. On the modeling side, uncertainties arise from the use of spatially generalized mineralogical source maps and from the treatment of emission, transport, and deposition processes. Additional uncertainty is introduced through the meteorological forcing provided by WRF, including wind fields, boundary-layer dynamics, and vertical mixing.

Acknowledging these aspects is essential for placing the results in context and for guiding future efforts aimed at improving the representation of desert dust composition and its impacts through enhanced observational–modeling synergy.

5 Appendices

Table A2. Conversion table linking key minerals to the average relative composition of major desert dust elements (including oxygen).

Mineral/Chemical elements	Na	Mg	Al	Si	S	K	Ca	Ti	Fe
Quartz-like				0.467					
Kaolinite-like			0.243	0.244				0.012	
Illite/ Muscovite-like		0.014	0.115	0.284		0.048	0.016	0.004	0.045
Smectite-like		0.015	0.105	0.335			0.011		0.031
Feldspar-like	0.011		0.127	0.287		0.058	0.045		
Calcite-like							0.400		
Gypsum-like					0.236		0.294		
Fe-oxide/ Fe-hydroxide-like			0.037	0.024					0.614

https://doi.org/10.5194/egusphere-2026-921
Preprint. Discussion started: 18 May 2026

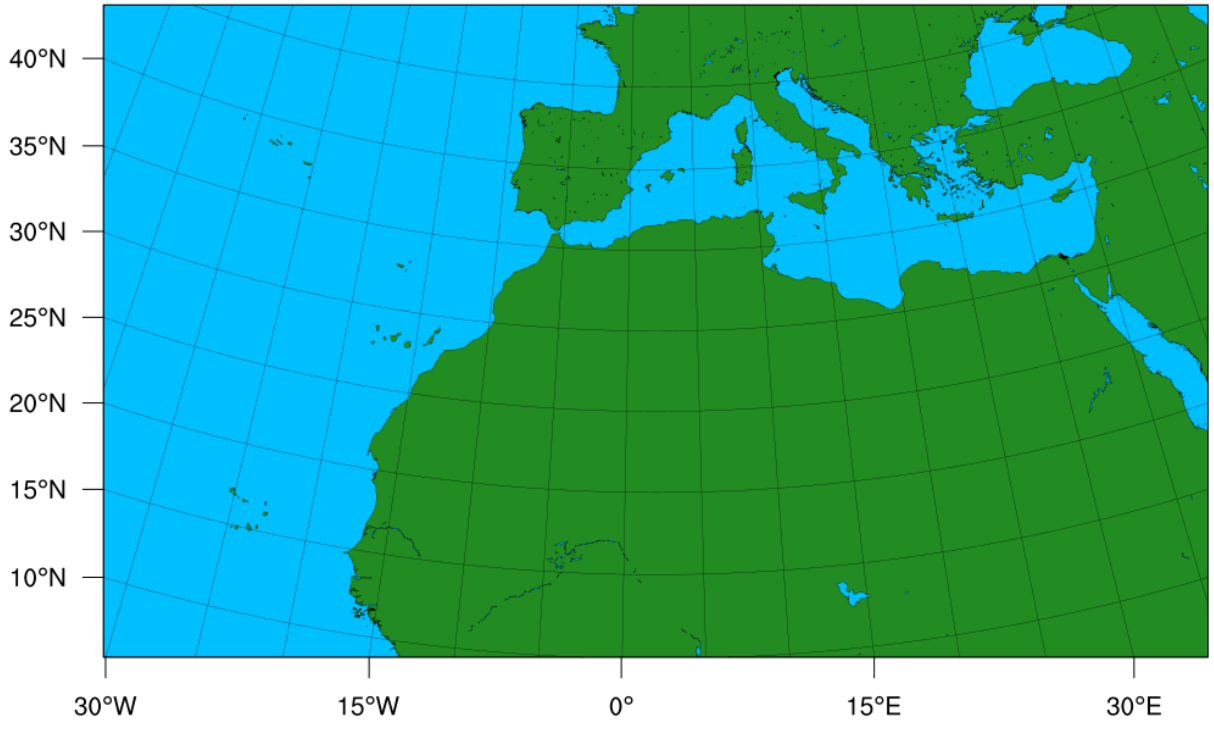

Figure A1. The domain of METAL-WRF used in the simulations

Table A2. Physical Schemes and Parameterizations used in the METAL-WRF setup

Parameterization	Scheme	Reference
Microphysics	Goddard microphysics scheme	(Tao et al., 2016)
Cumulus	Tiedtke scheme	(Zhang et al., 2011)
Shortwave/Shortwave radiation	RRTMG scheme	(Iacono et al., 2008)
Surface Layer	Eta similarity scheme	(Janjic, 1996, 2002)
Land Surface	Noah Land Surface Model	(Tewari et al., 2004)
Planetary Boundary layer	Mellor-Yamada-Janjic scheme	(Janjić, 1994; Mesinger, 1993)
Dust module	GOCART simple aerosol scheme	(Ginoux et al., 2001)
Dust emission scheme	AFWA	(LeGrand et al., 2019)

https://doi.org/10.5194/egusphere-2026-921
Preprint. Discussion started: 18 May 2026

Table A3. Overview of the air-masses origin of the in-situ measurement cases based on HYSPLIT backward trajectories.

Impactor identifier	Impactor sampling time (UTC)	Impactor sampling altitude range (m)	Air-Mass Origin Sector (Relative to Cabo Verde) (HYSPLIT)	Height of air mass (HYSPLIT)
A_03	11/6/2022 18:39-18:43	2400-3200	NE	< 1.5 km over land, 2 days prior
A_04	11/6/2022 18:45-18:47	1800-2200	NW	> 2 km over ocean
A_06	15/6/2022 12:37-12:40	2389-3126	SE, E	From SE, near surface over land, 5 days prior
A_07	15/6/2022 12:41-12:45	1255-2081	SE, NE, NW	From SE, near surface over land, 3-4 days prior
A_08	19/6/2022 18:33-18:36	1550-2399	NE, SE	From SE, near surface over land, 2 days prior
A_09	20/6/2022 5:25-5:27	2278-3025	NE	Near surface over land, 3 days prior
A_10	17/6/2022 18:15-18:20	2499-3384	E	Near surface over land, 4 days prior
A_11	26/6/2022 04:27-04:33	3151-4990	SE, E	> 2 km above land
A_12	23/6/2022 18:05-18:10	2097-3139	SE, E	From SE, near surface over land, 4 days prior
A_15	24/6/2022 18:56-19:01	3142-4789	E	> 1.5 km over land
A_16	24/6/2022 19:03-19:07	1596-2640	SE, S	From SE, near surface over land, 4 days prior
A_18	26/6/2022 04:33-04:38	1784-2894	SE, E	From SE, < 1 km over land, 3 days prior
C_02	28/6/2022 12:33-12:37	2308-3053	E	> 2 km over land
C_05	30/6/2022 04:31-04:36	2079-3126	E, NE	From NE, < 1 km over land, 5 days prior

https://doi.org/10.5194/egusphere-2026-921
Preprint. Discussion started: 18 May 2026

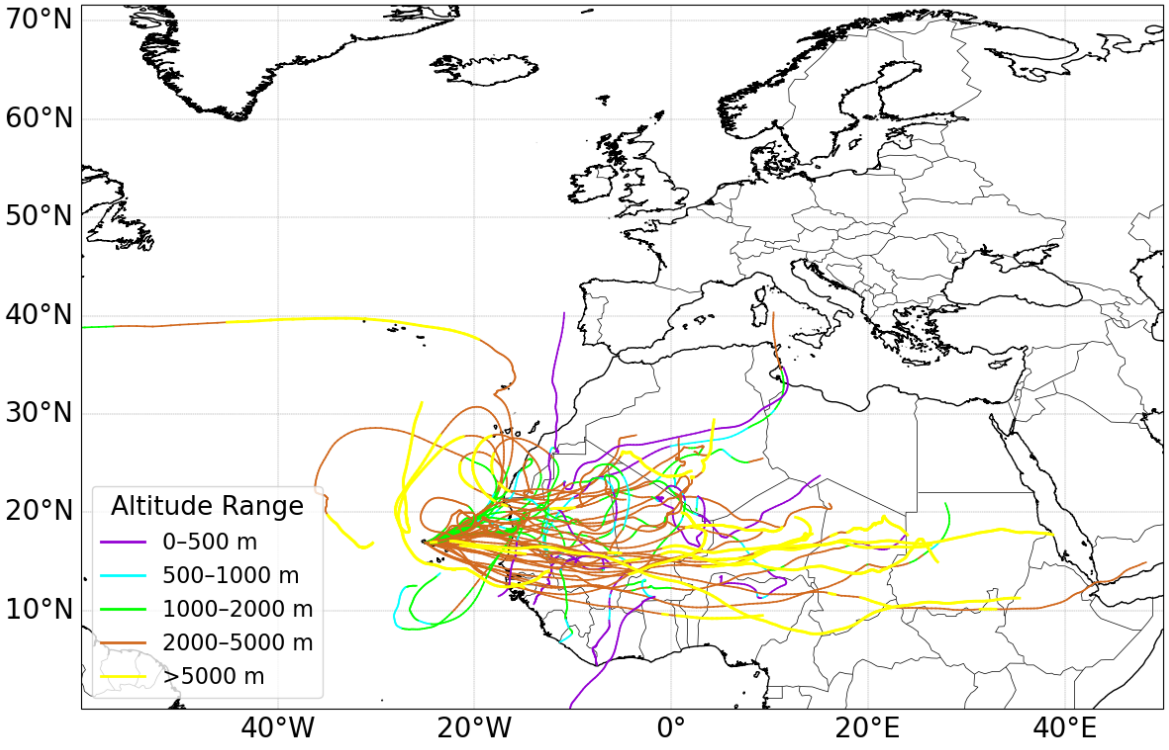

Figure A2. 8-day backward trajectories with HYSPLIT of air-masses observed over Mindelo during the period 11–30 June 2022. Different colors (changing within the same trajectory) indicate the altitude ranges through which the air-masses traveled.

https://doi.org/10.5194/egusphere-2026-921
Preprint. Discussion started: 18 May 2026

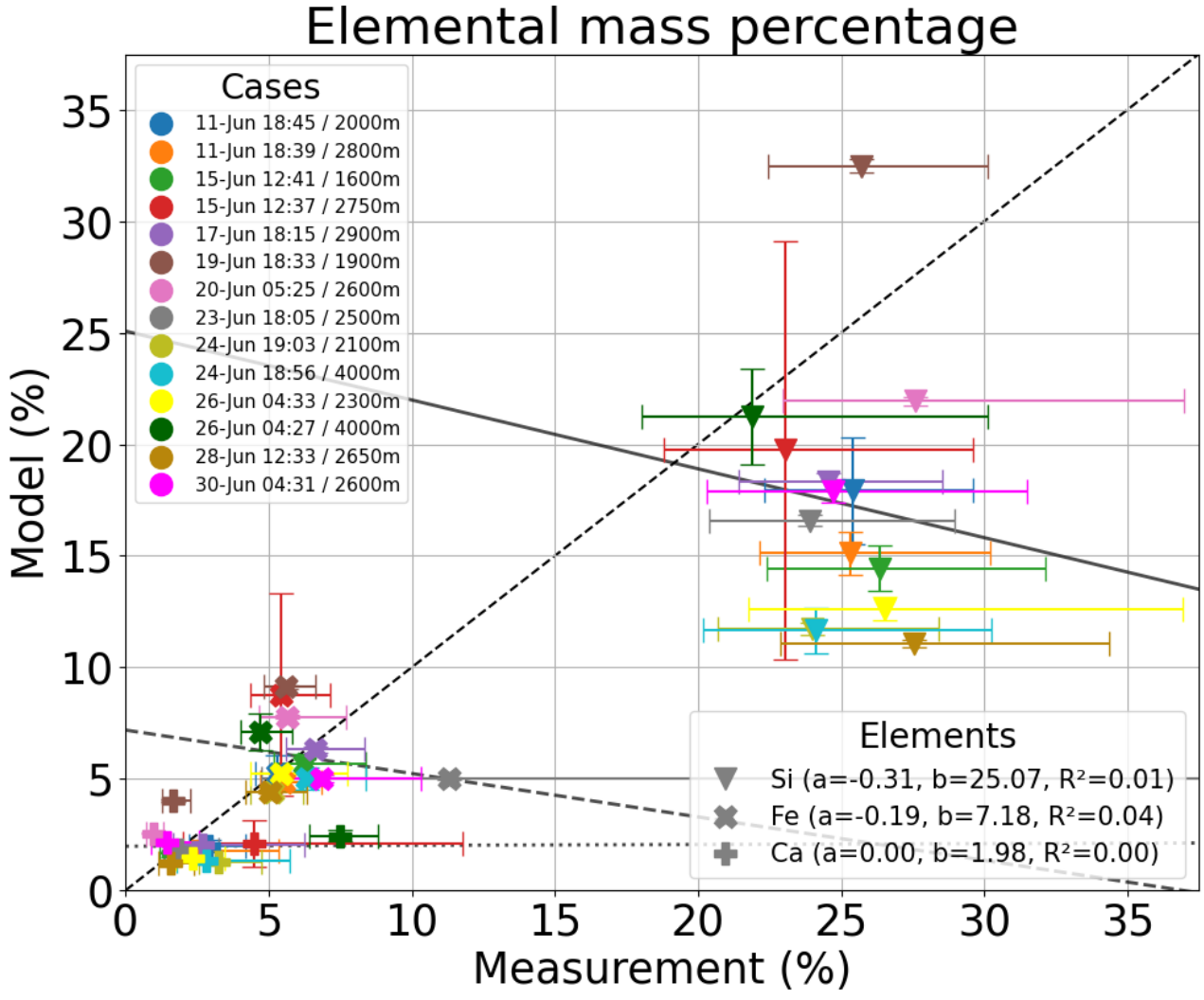

Figure A3. Scatter plot of in-situ measurements versus METAL-WRF model-derived elemental mass percentages for selected elements across all individual cases. Linear regression results are shown. Each case is labelled with the measurement time (June 2022, UTC), and the midpoint of the impactor sampling height range.

https://doi.org/10.5194/egusphere-2026-921
Preprint. Discussion started: 18 May 2026

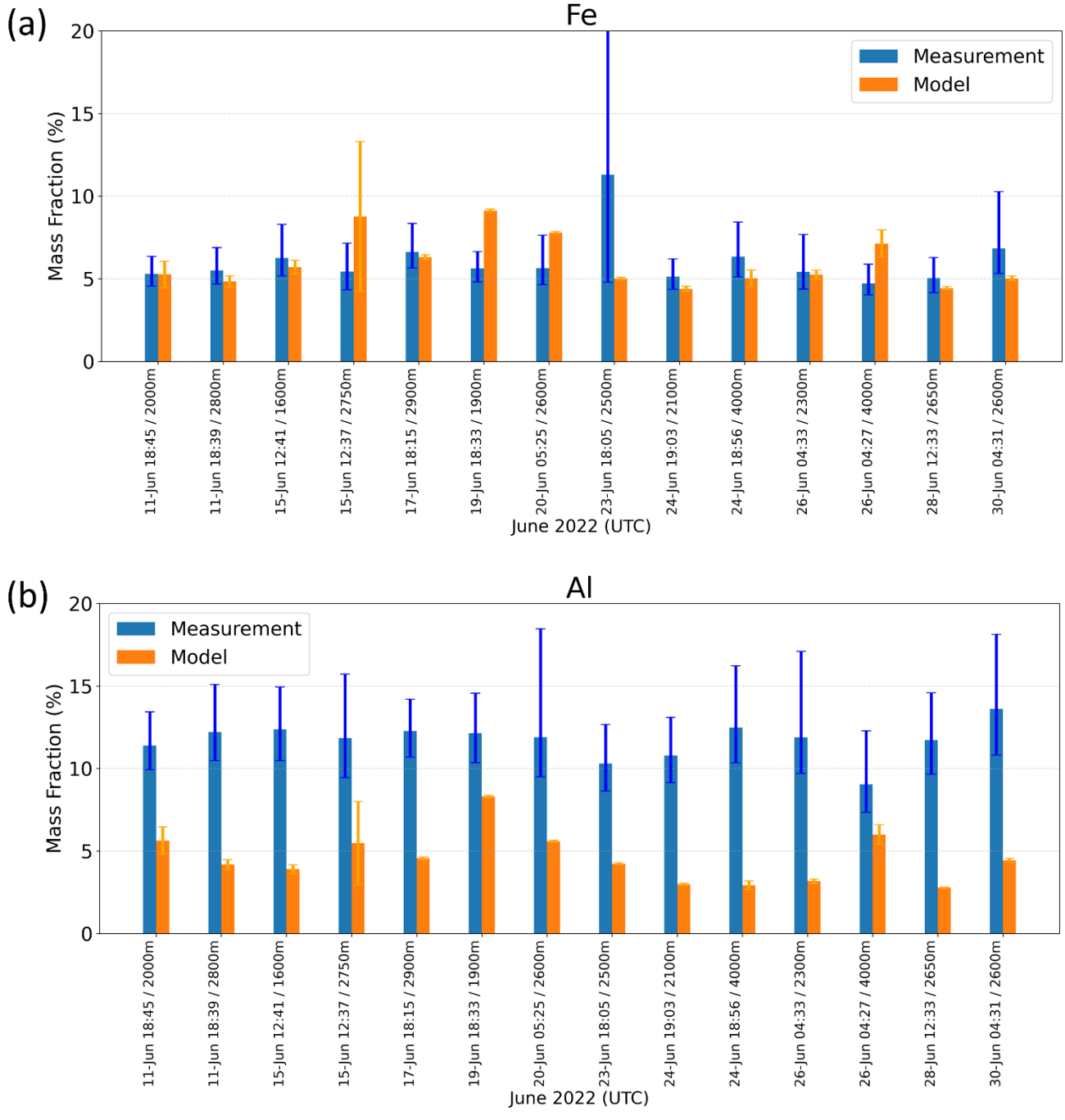

Figure A4. Temporal evolution of in-situ measurements versus METAL-WRF model-derived elemental mass percentages for (a) Fe and (b) Al over the observation period. The x-axis shows the measurement date and time and the midpoint of the impactor sampling height range for each case.

460

https://doi.org/10.5194/egusphere-2026-921
Preprint. Discussion started: 18 May 2026

Code and data availability

All algorithms were written with Python programming language, version 3.10, and can be obtained from the co-author Maria Tsichla (mtsichla@noa.gr) upon request. METAL-WRF model can be accessed upon request to the co-author Stavro Solomo. The HYSPLIT model is publicly available (https://www.ready.noaa.gov/hypub-bin/trajtype.pl?runtype=archive). The FLEXPART-WRF model code is publicly available and can be obtained from https://git.nilu.no/flexpart/flexpart-wrf (Brioude et al., 2013; Dingwell, 2025).

Author contributions

MT conceptualized the paper along with NM, AT and VA. All authors wrote parts of the paper corresponding to their work and respective results. KK and SA performed the filter analysis. SS and CS performed the METAL-WRF runs. AK performed the FLEXPART runs. MK, AP, FM and JS conducted the UAV flights and the in-situ measurements. All authors provided corrections and suggestions to eventually shape the research analysis, and final paper. MT supervised and directed the whole project.

Competing interests

At least one of the (co-)authors is a member of the editorial board of Atmospheric Measurement Techniques.

Acknowledgements

This work used data from the ASKOS campaign, which was funded by the ASKOS ESA project (contract nr. 4000131861/20/NL/IA), the D-TECT ERC Consolidator Grant (ERC-CoG grant agreement 725698) and the German Federal Ministry for Economic Affairs and Energy (BMWi) (grant no. 50EE1721C). We also acknowledge the Unmanned Systems Research Laboratory (USRL) of the Cyprus Institute for its support in the field deployment of the UAVs during the campaign. We thank Holger Baars, Ronny Engelmann and their staff for establishing and maintaining the AERONET site in Mindelo, which provided data used in this study. The authors further acknowledge the use of satellite data products provided by NASA, including AIRS Level 2 Dust Score and MODIS Corrected Reflectance datasets (AIRS2SUP_NRT, doi:10.5067/MOQOVNHNERGG; AIRS2SUP, doi:10.5067/APJ6EEN0PD0Z; MOD02QKM, doi:10.5067/MODIS/MOD02QKM.061; MOD02HKM, doi:10.5067/MODIS/MOD02HKM.061; MOD021KM, doi:10.5067/MODIS/MOD021KM.061; MYD02QKM, doi:10.5067/MODIS/MYD02QKM.061).

https://doi.org/10.5194/egusphere-2026-921
Preprint. Discussion started: 18 May 2026

Financial support

This work was supported by the PANGEA4CalVal project (GA 101079201), funded by the European Union; and services provided by the PANhellenic GEophysical observatory of Antikythera (PANGEA) of NOA and from COST Action EARLICOST, supported by COST (European Cooperation in Science and Technology). Additional funding was provided by the CERTAINTY project (Grant Agreement 101137680), funded under the Horizon Europe programme, by the PANORAMA project (Grant Agreement No. 101182795), funded by the European Union program and by the AIRSENSE (Aerosol and aerosol cloud Interaction from Remote SENSing Enhancement) project, funded from the European Space Agency (Contract No. 4000142902/23/I-NS). Also by the European Union's Horizon 2020 research and innovation programme under grant agreement No. 856612 and the Cyprus Government. Further support was provided through the ATMO-ACCESS Integrating Activity (Grant Agreement No 101008004).

References

Adebiyi, A. A., Huang, Y., Samset, B. H., and Kok, J. F.: Observations suggest that North African dust absorbs less solar radiation than models estimate, Commun. Earth Environ., 4, https://doi.org/10.1038/s43247-023-00825-2, 2023.

Atkinson, J. D., Murray, B. J., Woodhouse, M. T., Whale, T. F., Baustian, K. J., Carslaw, K. S., Dobbie, S., O'Sullivan, D., and Malkin, T. L.: The importance of feldspar for ice nucleation by mineral dust in mixed-phase clouds, Nature, 498, 355–358, https://doi.org/10.1038/nature12278, 2013.

Bauer, S. E., Balkanski, Y., Schulz, M., Hauglustaine, D. A., and Dentener, F.: Global modeling of heterogeneous chemistry on mineral aerosol surfaces: Influence on tropospheric ozone chemistry and comparison to observations, J. Geophys. Res.-Atmos., 109, https://doi.org/10.1029/2003JD003868, 2004.

Bieber, P., Seifried, T. M., Burkart, J., Gratzl, J., Kasper-Giebl, A., Schmale, D. G., and Grothe, H.: A Drone-Based Bioaerosol Sampling System to Monitor Ice Nucleation Particles in the Lower Atmosphere, Remote Sens., 12, 552, https://doi.org/10.3390/rs12030552, 2020.

Brioude, J., Arnold, D., Stohl, A., Cassiani, M., Morton, D., Seibert, P., Angevine, W., Evan, S., Dingwell, A., Fast, J. D., Easter, R. C., Pisso, I., Burkhart, J., and Wotawa, G.: The Lagrangian particle dispersion model FLEXPART-WRF version 3.1, Geosci. Model Dev., 6, 1889–1904, https://doi.org/10.5194/gmd-6-1889-2013, 2013.

Burgués, J. and Marco, S.: Environmental chemical sensing using small drones: A review, Sci. Total Environ., 748, 141172, https://doi.org/10.1016/j.scitotenv.2020.141172, 2020.

Chen, L., Peng, C., Gu, W., Fu, H., Jian, X., Zhang, H., Zhang, G., Zhu, J., Wang, X., and Tang, M.: On mineral dust aerosol hygroscopicity, Atmos. Chem. Phys., 20, 13611–13626, https://doi.org/10.5194/acp-20-13611-2020, 2020.

Cheng, M.-D., Chien, C.-H., Graham, D. E., and Harter, A.: Development of a microsampler suitable for aerial collection of aerosol particles, Environ. Sci.: Atmos., 3, 328–337, https://doi.org/10.1039/D2EA00096B, 2023.

https://doi.org/10.5194/egusphere-2026-921
Preprint. Discussion started: 18 May 2026

Chou, C., Formenti, P., Maille, M., Ausset, P., Helas, G., Harrison, M., and Osborne, S.: Size distribution, shape, and composition of mineral dust aerosols collected during the African Monsoon Multidisciplinary Analysis Special Observation Period 0: Dust and Biomass-Burning Experiment field campaign in Niger, January 2006, J. Geophys. Res.-Atmos., 113, https://doi.org/10.1029/2008JD009897, 2008.

Claquin, T., Schulz, M., and Balkanski, Y.: Modeling the mineralogy of atmospheric dust sources, J. Geophys. Res.-Atmos., 104, 22243–22256, https://doi.org/10.1029/1999JD900416, 1999.

Crazzolara, C., Ebner, M., Platis, A., Miranda, T., Bange, J., and Junginger, A.: A new multicopter-based unmanned aerial system for pollen and spores collection in the atmospheric boundary layer, Atmos. Meas. Tech., 12, 1581–1598, https://doi.org/10.5194/amt-12-1581-2019, 2019.

DeMott, P. J., Sassen, K., Poellot, M. R., Baumgardner, D., Rogers, D. C., Brooks, S. D., Prenni, A. J., and Kreidenweis, S. M.: African dust aerosols as atmospheric ice nuclei, Geophys. Res. Lett., 30, https://doi.org/10.1029/2003GL017410, 2003.

Desboeufs, K. V. and Cautenet, G.: Transport and mixing zone of desert dust and sulphate over Tropical Africa and the Atlantic Ocean region, Atmos. Chem. Phys. Discuss., 5, https://doi.org/10.5194/acpd-5-5615-2005, 2005.

Di Biagio, C., Formenti, P., Balkanski, Y., Caponi, L., Cazaunau, M., Pangui, E., Journet, E., Nowak, S., Andreae, M. O., Kandler, K., Saeed, T., Piketh, S., Seibert, D., Williams, E., and Doussin, J.-F.: Complex refractive indices and single-scattering albedo of global dust aerosols in the shortwave spectrum and relationship to size and iron content, Atmos. Chem. Phys., 19, 15503–15531, https://doi.org/10.5194/acp-19-15503-2019, 2019.

Dingwell, A.: FLEXPART-WRF code, NILU GitLab repository [code], https://git.nilu.no/flexpart/flexpart-wrf, last access: 10 July 2025, 2025.

Drenkard, E. J., John, J. G., Stock, C. A., Lim, H., Dunne, J. P., Ginoux, P., and Luo, J. Y.: The Importance of Dynamic Iron Deposition in Projecting Climate Change Impacts on Pacific Ocean Biogeochemistry, Geophys. Res. Lett., 50, https://doi.org/10.1029/2022GL102058, 2023.

Dubovik, O. and King, M. D.: A flexible inversion algorithm for retrieval of aerosol optical properties from Sun and sky radiance measurements, J. Geophys. Res.-Atmos., https://doi.org/10.1029/2000JD900282, 2000.

Dubovik, O., Sinyuk, A., Lapyonok, T., Holben, B. N., Mishchenko, M., Yang, P., Eck, T. F., Volten, H., Muñoz, O., Veihelmann, B., van der Zande, W. J., Leon, J.-F., Sorokin, M., and Slutsker, I.: Application of spheroid models to account for aerosol particle nonsphericity in remote sensing of desert dust, J. Geophys. Res.-Atmos., 111, https://doi.org/10.1029/2005JD006619, 2006.

Efron, B.: Second Thoughts on the Bootstrap, Stat. Sci., 18, https://doi.org/10.1214/ss/1063994968, 2003.

Engelstaedter, S. and Washington, R.: Temporal controls on global dust emissions: The role of surface gustiness, Geophys. Res. Lett., 34, https://doi.org/10.1029/2007GL029971, 2007.

Fehr, T., McCarthy, W., Amiridis, V., Baars, H., von Bismarck, J., Borne, M., Chen, S., Flamant, C., Marenco, F., Knipperz, P., Koopman, R., Lemmerz, C. L., Marinou, E., Močnik, G., Parrinello, T., Piña, A., Reitebuch, O., Skofronick-Jackson,

https://doi.org/10.5194/egusphere-2026-921
Preprint. Discussion started: 18 May 2026

G., Zawislak, J., and Zenk, C.: The Joint Aeolus Tropical Atlantic Campaign 2021/2022 Overview–Atmospheric Science and Satellite Validation in the Tropics, EGUsphere, https://doi.org/10.5194/egusphere-egu23-7249, 2023.

Fenter, P., Teng, H., Geissbühler, P., Hanchar, J. M., Nagy, K. L., and Sturchio, N. C.: Atomic-scale structure of the orthoclase (001)–water interface measured with high-resolution X-ray reflectivity, Geochim. Cosmochim. Acta, 64, 3663–3673, https://doi.org/10.1016/S0016-7037(00)00455-5, 2000.

Formenti, P., Caquineau, S., Desboeufs, K., Klaver, A., Chevaillier, S., Journet, E., and Rajot, J. L.: Mapping the physico-chemical properties of mineral dust in western Africa: mineralogical composition, Atmos. Chem. Phys., 14, 10663–10686, https://doi.org/10.5194/acp-14-10663-2014, 2014.

Formenti, P., Elbert, W., Maenhaut, W., Haywood, J., and Andreae, M. O.: Chemical composition of mineral dust aerosol during the Saharan Dust Experiment (SHADE) airborne campaign in the Cape Verde region, September 2000, J. Geophys. Res.-Atmos., 108, https://doi.org/10.1029/2002JD002648, 2003.

Fountoulakis, I., Tsekeri, A., Kazadzis, S., Amiridis, V., Nersesian, A., Tsichla, M., Proestakis, E., Gkikas, A., Papachristopoulou, K., Barlakas, V., Emde, C., and Mayer, B.: A sensitivity study on radiative effects due to the parameterization of dust optical properties in models, Atmos. Chem. Phys., 24, 4915–4948, https://doi.org/10.5194/acp-24-4915-2024, 2024.

Ginoux, P., Chin, M., Tegen, I., Prospero, J. M., Holben, B., Dubovik, O., and Lin, S.: Sources and distributions of dust aerosols simulated with the GOCART model, J. Geophys. Res.-Atmos., 106, 20255–20273, https://doi.org/10.1029/2000JD000053, 2001.

Glotch, T. D., Rossman, G. R., and Aharonson, O.: Mid-infrared (5–100 μm) reflectance spectra and optical constants of ten phyllosilicate minerals, Icarus, 192, 605–622, https://doi.org/10.1016/j.icarus.2007.07.002, 2007.

Gogoi, M. M., Thakur, R. C., Gazi, S., Nair, V. S., Mohan, R., and Babu, S. S.: Vertical distributions of the microscopic morphological characteristics and elemental composition of aerosols over India, J. Atmos. Chem., 77, 117–140, https://doi.org/10.1007/s10874-020-09406-5, 2020.

Grell, G. A., Peckham, S. E., Schmitz, R., McKeen, S. A., Frost, G., Skamarock, W. C., and Eder, B.: Fully coupled "online" chemistry within the WRF model, Atmos. Environ., 39, 6957–6975, https://doi.org/10.1016/j.atmosenv.2005.04.027, 2005.

Gustafsson, R. J., Orlov, A., Badger, C. L., Griffiths, P. T., Cox, R. A., and Lambert, R. M.: A comprehensive evaluation of water uptake on atmospherically relevant mineral surfaces: DRIFT spectroscopy, thermogravimetric analysis and aerosol growth measurements, Atmos. Chem. Phys., 5, 3415–3421, https://doi.org/10.5194/acp-5-3415-2005, 2005.

Hanisch, F. and Crowley, J. N.: Ozone decomposition on Saharan dust: an experimental investigation, Atmos. Chem. Phys., 3, 119–130, https://doi.org/10.5194/acp-3-119-2003, 2003.

Hanke, M., Umann, B., Uecker, J., Arnold, F., and Bunz, H.: Atmospheric measurements of gas-phase HNO3 and SO2 using chemical ionization mass spectrometry during the MINATROC field campaign 2000 on Monte Cimone, Atmos. Chem. Phys., 3, 417–436, https://doi.org/10.5194/acp-3-417-2003, 2003.

https://doi.org/10.5194/egusphere-2026-921
Preprint. Discussion started: 18 May 2026

Hatch, C. D., Greenaway, A. L., Christie, M. J., and Baltrusaitis, J.: Water adsorption constrained Frenkel–Halsey–Hill adsorption activation theory: Montmorillonite and illite, Atmos. Environ., 87, 26–33, https://doi.org/10.1016/j.atmosenv.2013.12.040, 2014.

Herbin, H., Deschutter, L., Deguine, A., and Petitprez, D.: Complex refractive index of crystalline quartz particles from UV to thermal infrared, Aerosol Sci. Technol., 57, 255–265, https://doi.org/10.1080/02786826.2023.2165899, 2023.

Hersbach, H., Bell, B., Berrisford, P., Hirahara, S., Horányi, A., Muñoz-Sabater, J., Nicolas, J., Peubey, C., Radu, R., Schepers, D., Simmons, A., Soci, C., Abdalla, S., Abellan, X., Balsamo, G., Bechtold, P., Biavati, G., Bidlot, J., Bonavita, M., and Thépaut, J.: The ERA5 global reanalysis, Q. J. Roy. Meteor. Soc., 146, 1999–2049, https://doi.org/10.1002/qj.3803, 2020.

Hess, M., Koepke, P., and Schult, I.: Optical Properties of Aerosols and Clouds: The Software Package OPAC, Bull. Amer. Meteor. Soc., 79, 831–844, https://doi.org/10.1175/1520-0477(1998)079<0831:OPOAAC>2.0.CO;2, 1998.

Hubert, P., Herbin, H., Visez, N., Pujol, O., and Petitprez, D.: New approach for the determination of aerosol refractive indices – Part II: Experimental set-up and application to amorphous silica particles, J. Quant. Spectrosc. Ra., 200, 320–327, https://doi.org/10.1016/j.jqsrt.2017.03.037, 2017.

Iacono, M. J., Delamere, J. S., Mlawer, E. J., Shephard, M. W., Clough, S. A., and Collins, W. D.: Radiative forcing by long-lived greenhouse gases: Calculations with the AER radiative transfer models, J. Geophys. Res.-Atmos., 113, https://doi.org/10.1029/2008JD009944, 2008.

Janjić, Z. I.: The Step-Mountain Eta Coordinate Model: Further Developments of the Convection, Viscous Sublayer, and Turbulence Closure Schemes, Mon. Weather Rev., 122, 927–945, https://doi.org/10.1175/1520-0493(1994)122%3c0927:TSMECM%3e2.0.CO;2, 1994.

Janjic, Z. I.: The surface layer in the NCEP Eta Model, Preprints, 11th Conf. on Numerical Weather Prediction, Norfolk, VA, Amer. Meteor. Soc., 354, 1996.

Janjic, Z. I.: Nonsingular implementation of the Mellor-Yamada Level 2.5 Scheme in the NCEP Meso model, NCEP Office Note, 436, 2002.

Jeong, G. Y., Park, M. Y., Kandler, K., Nousiainen, T., and Kemppinen, O.: Mineralogical properties and internal structures of individual fine particles of Saharan dust, Atmos. Chem. Phys., 16, 12397–12410, https://doi.org/10.5194/acp-16-12397-2016, 2016.

Jickells, T. D., An, Z. S., Andersen, K. K., Baker, A. R., Bergametti, G., Brooks, N., Cao, J. J., Boyd, P. W., Duce, R. A., Hunter, K. A., Kawahata, H., Kubilay, N., laRoche, J., Liss, P. S., Mahowald, N., Prospero, J. M., Ridgwell, A. J., Tegen, I., and Torres, R.: Global Iron Connections Between Desert Dust, Ocean Biogeochemistry, and Climate, Science, 308, 67–71, https://doi.org/10.1126/science.1105959, 2005.

Joshi, N., Romanias, M. N., Riffault, V., and Thevenet, F.: Investigating water adsorption onto natural mineral dust particles: Linking DRIFTS experiments and BET theory, Aeolian Res., 27, 35–45, https://doi.org/10.1016/j.aeolia.2017.06.001, 2017.

https://doi.org/10.5194/egusphere-2026-921
Preprint. Discussion started: 18 May 2026

Kandler, K., Benker, N., Bundke, U., Cuevas, E., Ebert, M., Knippertz, P., Rodríguez, S., Schütz, L., and Weinbruch, S.: Chemical composition and complex refractive index of Saharan Mineral Dust at Izaña, Tenerife (Spain) derived by electron microscopy, Atmos. Environ., 41, 8058–8074, https://doi.org/10.1016/j.atmosenv.2007.06.047, 2007.

Kandler, K., Schneiders, K., Ebert, M., Hartmann, M., Weinbruch, S., Prass, M., and Pöhlker, C.: Composition and mixing state of atmospheric aerosols determined by electron microscopy: method development and application to aged Saharan dust deposition in the Caribbean boundary layer, Atmos. Chem. Phys., 18, 13429–13455, https://doi.org/10.5194/acp-18-13429-2018, 2018.

Kezoudi, M., Keleshis, C., Antoniou, P., Biskos, G., Bronz, M., Constantinides, C., Desservettaz, M., Gao, R.-S., Girdwood, J., Harnetiaux, J., Kandler, K., Leonidou, A., Liu, Y., Lelieveld, J., Marenco, F., Mihalopoulos, N., Močnik, G., Neitola, K., Paris, J.-D., and Sciare, J.: The Unmanned Systems Research Laboratory (USRL): A New Facility for UAV-Based Atmospheric Observations, Atmosphere, 12, 1042, https://doi.org/10.3390/atmos12081042, 2021.

Kezoudi, M., Papetta, A., Kandler, K., Ryder, C. L., Leonidou, A., Keleshis, C., Stopford, C., Thornberry, T., Mamouri, R.-E., Sciare, J., and Marenco, F.: Microphysical and Compositional Differences Between Saharan and Middle Eastern Dust Revealed by UAS Observations, EGUsphere, https://doi.org/10.5194/egusphere-2025-5234, 2025.

Knippertz, P. and Stuut, J.-B. W.: Mineral dust: a key player in the earth system, Springer, 2014.

Kumar, P., Sokolik, I. N., and Nenes, A.: Measurements of cloud condensation nuclei activity and droplet activation kinetics of fresh unprocessed regional dust samples and minerals, Atmos. Chem. Phys., 11, 3527–3541, https://doi.org/10.5194/acp-11-3527-2011, 2011.

Laskina, O., Young, M. A., Kleiber, P. D., and Grassian, V. H.: Infrared extinction spectra of mineral dust aerosol: Single components and complex mixtures, J. Geophys. Res.-Atmos., 117, https://doi.org/10.1029/2012JD017756, 2012.

LeGrand, S. L., Polashenski, C., Letcher, T. W., Creighton, G. A., Peckham, S. E., and Cetola, J. D.: The AFWA dust emission scheme for the GOCART aerosol model in WRF-Chem v3.8.1, Geosci. Model Dev., 12, 131–166, https://doi.org/10.5194/gmd-12-131-2019, 2019.

Lelieveld, J., Butler, T. M., Crowley, J. N., Dillon, T. J., Fischer, H., Ganzeveld, L., Harder, H., Lawrence, M. G., Martinez, M., Taraborrelli, D., and Williams, J.: Atmospheric oxidation capacity sustained by a tropical forest, Nature, 452, 737–740, https://doi.org/10.1038/nature06870, 2008.

Li, L., Mahowald, N. M., Gonçalves Ageitos, M., Obiso, V., Miller, R. L., Pérez García-Pando, C., Di Biagio, C., Formenti, P., Brodrick, P. G., Clark, R. N., Green, R. O., Kokaly, R., Swayze, G., and Thompson, D. R.: Improved constraints on hematite refractive index for estimating climatic effects of dust aerosols, Commun. Earth Environ., 5, https://doi.org/10.1038/s43247-024-01441-4, 2024.

Li, L., Mahowald, N. M., Miller, R. L., Pérez García-Pando, C., Klose, M., Hamilton, D. S., Gonçalves Ageitos, M., Ginoux, P., Balkanski, Y., Green, R. O., Kalashnikova, O., Kok, J. F., Obiso, V., Paynter, D., and Thompson, D. R.: Quantifying the range of the dust direct radiative effect due to source mineralogy uncertainty, Atmos. Chem. Phys., 21, 3973–4005, https://doi.org/10.5194/acp-21-3973-2021, 2021.

https://doi.org/10.5194/egusphere-2026-921
Preprint. Discussion started: 18 May 2026

Lieke, K., Kandler, K., Scheuvens, D., Emmel, C., Von Glahn, C., Petzold, A., Weinzierl, B., Veira, A., Ebert, M., Weinbruch, S., and Schütz, L.: Particle chemical properties in the vertical column based on aircraft observations in the vicinity of Cape Verde Islands, Tellus B, 63, 497, https://doi.org/10.1111/j.1600-0889.2011.00553.x, 2011.

Mahowald, N. M., Baker, A. R., Bergametti, G., Brooks, N., Duce, R. A., Jickells, T. D., Kubilay, N., Prospero, J. M., and Tegen, I.: Atmospheric global dust cycle and iron inputs to the ocean, Global Biogeochem. Cy., 19, https://doi.org/10.1029/2004GB002402, 2005.

Mahowald, N., Ward, D. S., Kloster, S., Flanner, M. G., Heald, C. L., Heavens, N. G., Hess, P. G., Lamarque, J.-F., and Chuang, P. Y.: Aerosol Impacts on Climate and Biogeochemistry, Annu. Rev. Environ. Resour., 36, 45–74, https://doi.org/10.1146/annurev-environ-042009-094507, 2011.

Maring, H., Savoie, D. L., Izaguirre, M. A., Custals, L., and Reid, J. S.: Mineral dust aerosol size distribution change during atmospheric transport, J. Geophys. Res.-Atmos., 108, https://doi.org/10.1029/2002JD002536, 2003.

Marinou, E., Paschou, P., Tsikoudi, I., Tsekeri, A., Daskalopoulou, V., Kouklaki, D., Siomos, N., Spanakis-Misirlis, V., Voudouri, K. A., Georgiou, T., Drakaki, E., Kampouri, A., Papachristopoulou, K., Mavropoulou, I., Mallios, S., Proestakis, E., Gkikas, A., Koutsoupi, I., Raptis, I. P., and Amiridis, V.: An Overview of the ASKOS Campaign in Cabo Verde, Environ. Sci. Proc., 26, 200, https://doi.org/10.3390/environsciproc2023026200, 2023.

Martin, J. H. and Fitzwater, S. E.: Iron deficiency limits phytoplankton growth in the north-east Pacific subarctic, Nature, 331, 341–343, https://doi.org/10.1038/331341a0, 1988.

Matsuki, A., Iwasaka, Y., Shi, G., Zhang, D., Trochkine, D., Yamada, M., Kim, Y., Chen, B., Nagatani, T., Miyazawa, T., Nagatani, M., and Nakata, H.: Morphological and chemical modification of mineral dust: Observational insight into the heterogeneous uptake of acidic gases, Geophys. Res. Lett., 32, https://doi.org/10.1029/2005GL024176, 2005.

Mesinger, F.: Forecasting upper tropospheric turbulence within the framework of the Mellor-Yamada 2.5 closure, WMO, Res. Activ. Atmos. Ocean. Model., 18, 4.28–4.29, 1993.

Newbury, D. E. and Ritchie, N. W. M.: Is scanning electron microscopy/energy dispersive x-ray spectroscopy (SEM/EDS) quantitative? Effect of specimen shape, Proc. SPIE, 8036, 803602, https://doi.org/10.1117/12.881040, 2011.

Nickovic, S., Vukovic, A., and Vujadinovic, M.: Atmospheric processing of iron carried by mineral dust, Atmos. Chem. Phys., 13, 9169–9181, https://doi.org/10.5194/acp-13-9169-2013, 2013.

Nickovic, S., Vukovic, A., Vujadinovic, M., Djurdjevic, V., and Pejanovic, G.: Technical Note: High-resolution mineralogical database of dust-productive soils for atmospheric dust modeling, Atmos. Chem. Phys., 12, 845–855, https://doi.org/10.5194/acp-12-845-2012, 2012.

Panta, A., Kandler, K., Alastuey, A., González-Flórez, C., González-Romero, A., Klose, M., Querol, X., Reche, C., Yus-Díez, J., and Pérez García-Pando, C.: Insights into the single-particle composition, size, mixing state, and aspect ratio of freshly emitted mineral dust from field measurements in the Moroccan Sahara using electron microscopy, Atmos. Chem. Phys., 23, 3861–3885, https://doi.org/10.5194/acp-23-3861-2023, 2023.

https://doi.org/10.5194/egusphere-2026-921
Preprint. Discussion started: 18 May 2026

Pérez García-Pando, C., Miller, R. L., Perlwitz, J. P., Rodríguez, S., and Prospero, J. M.: Predicting the mineral composition of dust aerosols: Insights from elemental composition measured at the Izaña Observatory, Geophys. Res. Lett., 43, https://doi.org/10.1002/2016GL069873, 2016.

Perlwitz, J. P., Pérez García-Pando, C., and Miller, R. L.: Predicting the mineral composition of dust aerosols – Part 2: Model evaluation and identification of key processes with observations, Atmos. Chem. Phys., 15, 11629–11652, https://doi.org/10.5194/acp-15-11629-2015, 2015.

Prospero, J. M., Ginoux, P., Torres, O., Nicholson, S. E., and Gill, T. E.: Environmental characterization of global sources of atmospheric soil dust identified with the Nimbus 7 Total Ozone Mapping Spectrometer (TOMS) absorbing aerosol product, Rev. Geophys., 40, https://doi.org/10.1029/2000RG000095, 2002.

Rodriguez-Navarro, C., di Lorenzo, F., and Elert, K.: Mineralogy and physicochemical features of Saharan dust wet deposited in the Iberian Peninsula during an extreme red rain event, Atmos. Chem. Phys., 18, 10089–10122, https://doi.org/10.5194/acp-18-10089-2018, 2018.

Ryder, C. L., Highwood, E. J., Lai, T. M., Sodemann, H., and Marsham, J. H.: Impact of atmospheric transport on the evolution of microphysical and optical properties of Saharan dust, Geophys. Res. Lett., 40, 2433–2438, https://doi.org/10.1002/Grl.50482, 2013.

Schuster, G. L., Dubovik, O., and Holben, B. N.: Angstrom exponent and bimodal aerosol size distributions, J. Geophys. Res.-Atmos., 111, https://doi.org/10.1029/2005JD006328, 2006.

Seinfeld, J. H. and Pandis, S. N.: Atmospheric Chemistry and Physics: From Air Pollution to Climate Change, John Wiley & Sons, 1998.

Shaw, P.: Application of aerosol speciation data as an in situ dust proxy for validation of the Dust Regional Atmospheric Model (DREAM), Atmos. Environ., 42, 7304–7309, https://doi.org/10.1016/j.atmosenv.2008.06.018, 2008.

Skamarock, W., Klemp, J., Dudhia, J., Gill, D. O., Liu, Z., Berner, J., Wang, W., Powers, J. G., Duda, M. G., Barker, D., and Huang, X.-Y.: A Description of the Advanced Research WRF Model Version 4.1, 2021.

Smith, H. R., Ulanowski, Z., Kaye, P. H., Hirst, E., Stanley, W., Kaye, R., Wieser, A., Stopford, C., Kezoudi, M., Girdwood, J., Greenaway, R., and Mackenzie, R.: The Universal Cloud and Aerosol Sounding System (UCASS): a low-cost miniature optical particle counter for use in dropsonde or balloon-borne sounding systems, Atmos. Meas. Tech., 12, 6579–6599, https://doi.org/10.5194/amt-12-6579-2019, 2019.

Solomos, S., Kallos, G., Kushta, J., Astitha, M., Tremback, C., Nenes, A., and Levin, Z.: An integrated modeling study on the effects of mineral dust and sea salt particles on clouds and precipitation, Atmos. Chem. Phys., 11, 873–892, https://doi.org/10.5194/acp-11-873-2011, 2011.

Solomos, S., Spyrou, C., Barreto, A., Rodríguez, S., González, Y., Neophytou, M. K. A., Mouzourides, P., Bartsotas, N. S., Kalogeri, C., Nickovic, S., Vukovic Vimic, A., Vujadinovic Mandic, M., Pejanovic, G., Cvetkovic, B., Amiridis, V., Sykioti, O., Gkikas, A., and Zerefos, C.: The Development of METAL-WRF Regional Model for the Description of Dust Mineralogy in the Atmosphere, Atmosphere, 14, 1615, https://doi.org/10.3390/atmos14111615, 2023.

https://doi.org/10.5194/egusphere-2026-921
Preprint. Discussion started: 18 May 2026

Song, Q., Ginoux, P., Gonçalves Ageitos, M., Miller, R. L., Obiso, V., and Pérez García-Pando, C.: Modeling impacts of dust mineralogy on fast climate response, Atmos. Chem. Phys., 24, 7421–7446, https://doi.org/10.5194/acp-24-7421-2024, 2024.

Spyrou, C., Fountoulakis, I., Solomos, S., Papadimitriou, N., Bais, A., Gröbner, J., Meloni, D., and Zerefos, C.: Implications of dust minerals on radiative transfer at regional scale, using the METAL-WRF model, Atmos. Meas. Tech., 18, 7717–7734, https://doi.org/10.5194/amt-18-7717-2025, 2025.

Spyrou, C., Mitsakou, C., Kallos, G., Louka, P., and Vlastou, G.: An improved limited area model for describing the dust cycle in the atmosphere, J. Geophys. Res., 115, D17211, 2010.

Stein, A. F., Draxler, R. R., Rolph, G. D., Stunder, B. J. B., Cohen, M. D., and Ngan, F.: NOAA's HYSPLIT Atmospheric Transport and Dispersion Modeling System, Bull. Amer. Meteor. Soc., 96, 2059–2077, https://doi.org/10.1175/BAMS-D-14-00110.1, 2015.

Tang, M., Cziczo, D. J., and Grassian, V. H.: Interactions of Water with Mineral Dust Aerosol: Water Adsorption, Hygroscopicity, Cloud Condensation, and Ice Nucleation, Chem. Rev., 116, 4205–4259, https://doi.org/10.1021/acs.chemrev.5b00529, 2016.

Tao, W., Wu, D., Lang, S., Chern, J., Peters-Lidard, C., Fridlind, A., and Matsui, T.: High-resolution NU-WRF simulations of a deep convective-precipitation system during MC3E: Further improvements and comparisons between Goddard microphysics schemes and observations, J. Geophys. Res.-Atmos., 121, 1278–1305, https://doi.org/10.1002/2015JD023986, 2016.

Tewari, M., Chen, F., Wang, W., Dudhia, J., LeMone, M. A., Mitchell, K., Ek, M., Gayno, G., Wegiel, J., and Cuenca, R. H.: Implementation and verification of the unified NOAH land surface model in the WRF model, 20th Conference on Weather Analysis and Forecasting/16th Conference on Numerical Weather Prediction, 11–15, 2004.

Toledano, C., Wiegner, M., Garhammer, M., Seefeldner, M., Gasteiger, J., Müller, D., and Koepke, P.: Spectral aerosol optical depth characterization of desert dust during SAMUM 2006, Tellus B, 61, 216, https://doi.org/10.1111/j.1600-0889.2008.00382.x, 2009.

Tripathi, N., Krumm, B. E., Edtbauer, A., Ringsdorf, A., Wang, N., Kohl, M., Vella, R., Machado, L. A. T., Pozzer, A., Lelieveld, J., and Williams, J.: Impacts of convection, chemistry, and forest clearing on biogenic volatile organic compounds over the Amazon, Nat. Commun., 16, 4692, https://doi.org/10.1038/s41467-025-59953-2, 2025.

Tsarpalis, K., Papadopoulos, A., Mihalopoulos, N., Spyrou, C., Michaelides, S., and Katsafados, P.: The Implementation of a Mineral Dust Wet Deposition Scheme in the GOCART-AFWA Module of the WRF Model, Remote Sens., 10, 1595, https://doi.org/10.3390/rs10101595, 2018.

Tsichla, M., Tsekeri, A., Kezoudi, M., Kandler, K., Aryasree, S., Haarig, M., Baars, H., Gialitaki, A., Marinou, E., Marenco, F., Papetta, A., Sciare, J., Floutsi, A. A., Voudouri, K. A., Mihalopoulos, N., and Amiridis, V.: Quantifying dust concentration and internal mineralogical mixture, by combining remote sensing and airborne in-situ observations, during ASKOS, in preparation, 2026.

https://doi.org/10.5194/egusphere-2026-921
Preprint. Discussion started: 18 May 2026

Weger, M., Heinold, B., Engler, C., Schumann, U., Seifert, A., Fößig, R., Voigt, C., Baars, H., Blahak, U., Borrmann, S., Hoose, C., Kaufmann, S., Krämer, M., Seifert, P., Senf, F., Schneider, J., and Tegen, I.: The impact of mineral dust on cloud formation during the Saharan dust event in April 2014 over Europe, Atmos. Chem. Phys., 18, 17545–17572, https://doi.org/10.5194/acp-18-17545-2018, 2018.

Yakobi-Hancock, J. D., Ladino, L. A., and Abbatt, J. P. D.: Feldspar minerals as efficient deposition ice nuclei, Atmos. Chem. Phys., 13, 11175–11185, https://doi.org/10.5194/acp-13-11175-2013, 2013.

Yasar, M., Lai, A. M., de Foy, B., Schauer, J. J., Arhami, M., and Hosseini, V.: Chemical speciation of PM2.5 in Tehran: Quantification of dust contribution and model validation, Atmos. Pollut. Res., 11, 1839–1846, https://doi.org/10.1016/j.apr.2020.07.020, 2020.

Zhang, C., Wang, Y., and Hamilton, K.: Improved Representation of Boundary Layer Clouds over the Southeast Pacific in ARW-WRF Using a Modified Tiedtke Cumulus Parameterization Scheme, Mon. Weather Rev., 139, 3489–3513, https://doi.org/10.1175/MWR-D-10-05091.1, 2011.

Zimmermann, F., Weinbruch, S., Schütz, L., Hofmann, H., Ebert, M., Kandler, K., and Worringen, A.: Ice nucleation properties of the most abundant mineral dust phases, J. Geophys. Res.-Atmos., 113, https://doi.org/10.1029/2008jd010655, 2008.